universe

MDPI

Tutorial

A Tutorial on the Strong Gravity Effects in Black Hole X-Ray Spectra

Cosimo Bambi [1,2]

[1] Department of Physics, Center for Astronomy and Astrophysics, Center for Field Theory and Particle Physics, Fudan University, Shanghai 200438, China; bambi@fudan.edu.cn
[2] School of Natural Sciences and Humanities, New Uzbekistan University, Tashkent 100007, Uzbekistan

Abstract: This is a tutorial on the strong gravity effects (motion of massive and massless particles in a curved spacetime, evaluation of redshift factors, estimate of physical quantities in different reference frames, etc.) necessary to calculate the electromagnetic spectra of geometrically thin and optically thick accretion disks around black holes. The presentation is intentionally pedagogical, and most calculations are reported step by step. In the disk–corona model, the spectrum of a source has three components: a thermal component from the disk, a Comptonized component from the corona, and a reflection component from the disk. This tutorial reviews only the strong gravity effects, which can be decoupled from the physical processes involving the interaction between matter and radiation. The formulas presented here are valid for stationary, axisymmetric, asymptotically flat, circular spacetimes, so they can be potentially used for a large class of black hole solutions.

Keywords: black holes; accretion disks; X-ray astronomy; reflection models

check for updates

Citation: Bambi, C. A Tutorial on the Strong Gravity Effects in Black Hole X-Ray Spectra. *Universe* **2024**, *10*, 451. https://doi.org/10.3390/universe10120451

Academic Editors: Luka Č. Popović, Alexander F. Zakharov and Francesco De Paolis

Received: 16 October 2024
Revised: 1 December 2024
Accepted: 4 December 2024
Published: 8 December 2024

1. Introduction

The development of sufficiently advanced astrophysical models is crucial if we want to analyze high-quality data. The aim of this tutorial is to review the relativistic calculations of the electromagnetic spectrum of thin accretion disks around black holes.

The physical system that we want to study is shown in the left panel of Figure 1 and is normally referred to as the *disk–corona model*. The black hole can be either a stellar-mass black hole in an X-ray binary or a supermassive black hole in an active galactic nucleus. The key point is that the black hole accretes from a cold, geometrically thin, and optically thick accretion disk[1]. The disk is "cold" because it can efficiently emit radiation. Every point on the surface of the accretion disk has a blackbody-like spectrum, and the whole accretion disk has a multi-temperature blackbody-like spectrum. The thermal spectrum of the disk is normally peaked in the soft X-ray band (0.1–10 keV) for stellar-mass black holes in X-ray binaries and in the UV band (1–100 eV) for supermassive black holes in active galactic nuclei [1,2]. The *corona* (yellow regions in Figure 1) is some "hot" (∼100 keV), usually optically thin, cloud close to the black hole and the inner part of the accretion disk, but its exact morphology is not yet well understood [3–10]. The right panel in Figure 1 shows possible coronal geometries. In the lamppost model, the corona is a compact source along the black hole spin axis (for example, the base of the jet may act as a lamppost corona [7]). In the sandwich model, the corona is the hot atmosphere above the accretion disk [4,8,10]. In the spherical and toroidal models, the corona is the hot material in the plunging region, between the inner edge of the accretion disk and the black hole [4]. Compact coronae have been found from the study of reverberation lags in black hole X-ray binaries [11] and from the gravitational microlensing of quasars [12]. The coronal geometry can change (even on timescales of the order of hours or days in the case of X-ray binaries) [13], and two or more coronae may coexist at the same time.

Since the disk is cold and the corona is hot, thermal photons from the disk (red arrows in Figure 1) can inverse the Compton scatter off free electrons in the corona. The spectrum

of the Comptonized photons can be normally approximated well by a power law with a low- and a high-energy cutoff [5,14,15]. A fraction of the Comptonized photons (blue arrows in Figure 1) can illuminate the disk: Compton scattering and absorption followed by fluorescent emission produce the reflection spectrum (green arrows in Figure 1).

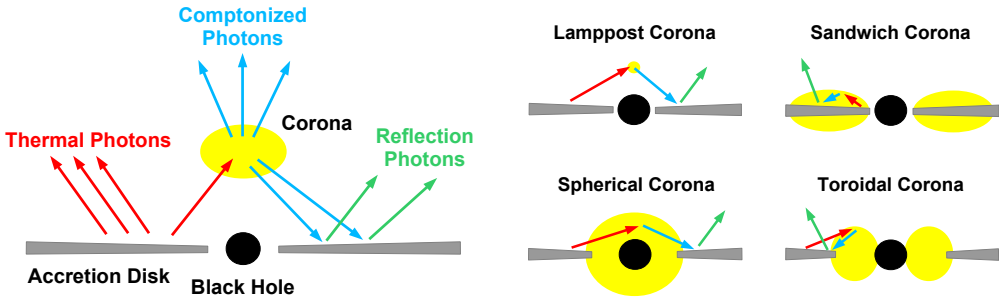

Figure 1. Left panel: Disk–corona model. **Right panel**: Examples of possible coronal geometries. See the text for more details. Figure from Ref. [16].

The reflection spectrum in the rest-frame of the material in the disk is characterized by narrow fluorescent emission lines in the soft X-ray band and a Compton hump with a peak around 20–40 keV [17,18]. The strongest emission feature is often the iron Kα complex, which is a very narrow feature at 6.4 keV in the case of neutral or weakly ionized iron atoms and shifts up to 6.97 keV in the case of H-like iron ions. The reflection spectrum of the whole disk as seen far from the source is blurred because of relativistic effects (Doppler boosting due to the motion of the material in the disk and gravitational redshift due to the gravitational well of the black hole) [19–22]. *X-ray reflection spectroscopy* is the analysis of these relativistically blurred reflection features in the X-ray spectra of X-ray binary systems and active galactic nuclei and can be a powerful tool to study the accretion process around black holes, measure black hole spins [23–25], and test Einstein's theory of general relativity in the strong field regime [26–28].

In these notes, we assume that the spacetime is stationary, axisymmetric, asymptotically flat, and circular. In spherical-like coordinates (t, r, θ, ϕ), the line element can always be written in the following form:

$$ds^2 = g_{tt}dt^2 + 2g_{t\phi}dt\,d\phi + g_{rr}dr^2 + g_{\theta\theta}d\theta^2 + g_{\phi\phi}d\phi^2\,, \tag{1}$$

where the metric coefficients are independent of the coordinates t and ϕ. The fact that the only non-vanishing off-diagonal element is $g_{t\phi}$ is a consequence of the assumption that the spacetime is *circular* [29,30]. Without such an assumption, in general, we may have other non-vanishing off-diagonal metric coefficients. In general relativity, $R_{\mu\nu} = 0$ in vacuum, and we can always write the line element as in Equation (1) for vacuum solutions if the spacetime is stationary and axisymmetric [30].

In these notes, we employ units in which $G_{\rm N} = c = \hbar = 1$, unless stated otherwise, and the convention of a metric with signature $(-+++)$.

1.1. Basic Concepts

It is useful to start reviewing some basic concepts. For the moment, we ignore the relativistic effects. Let us consider a detector and a source as shown in the left panel in Figure 2. The detector and the source are in empty space, so there is no absorption, scattering, or emission of radiation along the path from the source to the detector. Moreover, the size of the detector, the size of the source, and the distance between the source and the detector are much larger than the wavelength of the radiation emitted by the source, so we can use the *ray optics approximation*, where the radiated energy flows in straight lines. θ is the angle between the straight line connecting the detector and the source and the normal

to the surface of the detector. The energy dE illuminating the infinitesimal surface $d\sigma$ of the detector from the solid angle $d\Omega$ in the time dt and in the frequency band of width $d\nu$ is

$$dE = I_\nu \cos\theta \, d\sigma \, d\Omega \, dt \, d\nu \,, \tag{2}$$

where we introduced the *specific intensity* of the radiation I_ν, which is thus defined as

$$I_\nu = \frac{dE}{(\cos\theta \, d\sigma) d\Omega \, dt \, d\nu} \,. \tag{3}$$

The specific intensity can be measured, for example, in W m^{-2} Hz^{-1} sr^{-1}. The *total intensity* is obtained after integrating the specific intensity over all frequencies

$$I = \int_0^\infty I_\nu \, d\nu \,. \tag{4}$$

The total intensity can be measured, for example, in W m^{-2} sr^{-1}.

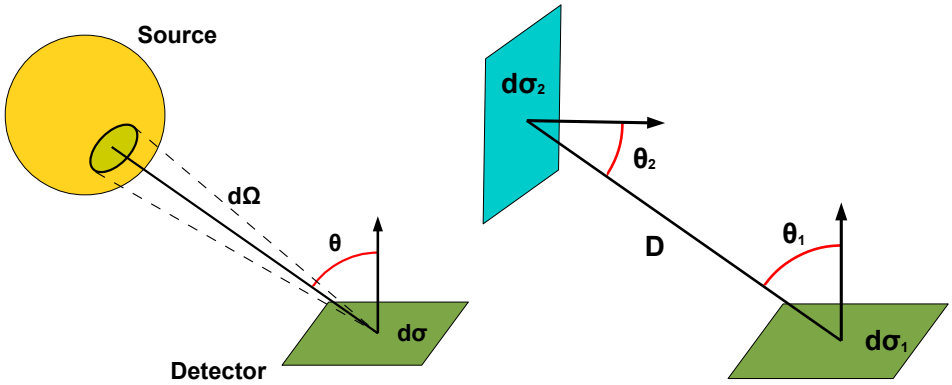

Figure 2. Left panel: The source illuminates the detector and deposits the energy dE on the surface $d\sigma$ of the detector from the solid angle $d\Omega$ in the time dt and in the frequency band of width $d\nu$: $dE = I_\nu \cos\theta \, d\sigma \, d\Omega \, dt \, d\nu$. **Right panel**: the specific intensity I_ν and the total intensity I are conserved along photon trajectories in empty space. See the text for more details. Figure from Ref. [16].

From our definition of specific intensity and total intensity, these two quantities are conserved along photon trajectories in empty space. Let us consider two infinitesimal surfaces, $d\sigma_1$ and $d\sigma_2$, as shown in the right panel in Figure 2. D is the distance between $d\sigma_1$ and $d\sigma_2$. $d\Omega_1 = \cos\theta_2 d\sigma_2 / D^2$ is the infinitesimal solid angle subtended by $d\sigma_2$ as seen from the surface $d\sigma_1$, and $d\Omega_2 = \cos\theta_1 d\sigma_1 / D^2$ is the infinitesimal solid angle subtended by $d\sigma_1$ as seen from the surface $d\sigma_2$. The power dE_1/dt in the frequency range ν to $\nu + d\nu$ flowing through the surface $d\sigma_1$ in the solid angle $d\Omega_1$ is

$$\frac{dE_1}{dt} = I_\nu^1 \cos\theta_1 \, d\Omega_1 \, d\sigma_1 \, d\nu = I_\nu^1 \cos\theta_1 \, \frac{\cos\theta_2 \, d\sigma_2}{D^2} \, d\sigma_1 \, d\nu \,, \tag{5}$$

where I_ν^1 is the specific intensity on $d\sigma_1$. In the same way, the power dE_2/dt in the frequency range ν to $\nu + d\nu$ flowing through the surface $d\sigma_2$ in the solid angle $d\Omega_2$ is

$$\frac{dE_2}{dt} = I_\nu^2 \cos\theta_2 \, d\Omega_2 \, d\sigma_2 \, d\nu = I_\nu^2 \cos\theta_2 \, \frac{\cos\theta_1 \, d\sigma_1}{D^2} \, d\sigma_2 \, d\nu \,. \tag{6}$$

Since there is no absorption/emission between the infinitesimal surfaces $d\sigma_1$ and $d\sigma_2$, $dE_1 = dE_2$, therefore $I_\nu^1 = I_\nu^2$, i.e., the specific intensity is conserved. We can repeat the calculations for the total intensity and arrive at the same conclusion.

If we integrate the specific intensity over the solid angle subtended by the source, we find the *spectral flux* (also called the spectral flux density or the flux density)

$$F_\nu = \int_{\text{source}} I_\nu \cos\theta \, d\Omega \,. \tag{7}$$

The spectral flux can be measured, for example, in W m^{-2} Hz^{-1}. The *total flux* is obtained after integrating the spectral flux over all frequencies

$$F = \int_0^\infty F_\nu \, d\nu \,. \tag{8}$$

The total flux can be measured, for example, in W m^{-2}.

The *spectral luminosity* is the total power per unit bandwidth emitted by the source at a certain frequency. It can be indicated with L_ν and can be measured, for example, in W Hz^{-1}. In general, it is not straightforward to measure the spectral luminosity of an astrophysical source if its emission is not isotropic. For an isotropic source at distance D, the spectral luminosity is

$$L_\nu = 4\pi D^2 \, F_\nu \,. \tag{9}$$

The *total luminosity* (also called the bolometric luminosity) is obtained after integrating the spectral luminosity over all frequencies

$$L = \int_0^\infty L_\nu \, d\nu \,. \tag{10}$$

The total luminosity can be measured, for example, in W.

Before concluding this subsection, it can be useful to stress a few important properties of the quantities discussed here:

1. The specific intensity I_ν is independent of the distance of the source $I_\nu =$ constant, while the spectral flux F_ν is proportional to the inverse of the square of the distance $F_\nu \propto D^{-2}$.
2. The specific intensity I_ν can be seen as the energy flowing out of the source as well as the energy flowing into the detector and, in general, as the energy flowing along any photon trajectory.
3. If a source is unresolved (i.e., it appears as a point-like source because its angular size is smaller than the angular resolution of the instrument used for its observation), we can measure the spectral flux F_ν, but we cannot measure the specific intensity I_ν.

1.2. Relativistic Effects

If the astrophysical source is a compact object, like a black hole or a neutron star, relativistic effects may not be ignored. Some results discussed in the previous subsection may require modifications.

If the wavelength of the radiation λ is much smaller than the size of the source, the size of the detector, and the distance between the source and the detector, we can still use the ray optics approximation, but in a curved spacetime, the radiated energy flows along null geodesics, which may not be straight lines.

The specific intensity I_ν and the total intensity I are not conserved along the photon trajectories. *Liouville's theorem* shows that the conserved quantity is instead I_ν/ν^3 (for the details, see Ref. [31]). If $I_{\rm e}(\nu_{\rm e})$ is the specific intensity at the emission point at the frequency $\nu_{\rm e}$ as measured in the rest-frame of the emitter, and $I_{\rm o}(\nu_{\rm o})$ is the specific intensity at the detection point at the frequency $\nu_{\rm o}$ as measured by the observer, the relation between these two specific intensities is

$$I_{\rm o}(\nu_{\rm o}) = g^3 I_{\rm e}(\nu_{\rm e}) \,, \tag{11}$$

where $g = \nu_o/\nu_e$ is the redshift factor between the detector and the emitter. If relativistic effects are negligible, $g = 1$, and we recover the result of the previous subsection.

2. Thin Accretion Disk

In this section, we present a simple model to describe thin, Keplerian accretion disks. The key assumptions are that the disk is non-self-gravitating[2] and that the motion of the material in the disk is determined by the gravitational field of the black hole, while other effects (for instance, the pressure of the material itself or the presence of magnetic fields) can be neglected. This implies that the motion of the accreting material is governed by the geodesic equations in the black hole spacetime.

2.1. Motion in a Stationary and Axisymmetric Spacetime

We assume that the motion of the "material"[3] in the accretion disk is determined by the gravitational field of the black hole, and therefore it can be derived from the Lagrangian of a point-like free particle

$$\mathcal{L} = \frac{1}{2}\left(g_{tt}\dot{t}^2 + 2g_{t\phi}\dot{t}\dot{\phi} + g_{rr}\dot{r}^2 + g_{\theta\theta}\dot{\theta}^2 + g_{\phi\phi}\dot{\phi}^2\right), \tag{12}$$

where $\dot{} = d/d\tau$, and τ is the proper time of the material. Since the metric coefficients are independent of the coordinates t and ϕ, we have two constants of motion: the specific energy E and the axial component of the specific angular momentum L_z:[4]

$$p_t = \frac{\partial \mathcal{L}}{\partial \dot{t}} = g_{tt}\dot{t} + g_{t\phi}\dot{\phi} = -E\,, \tag{13}$$

$$p_\phi = \frac{\partial \mathcal{L}}{\partial \dot{\phi}} = g_{t\phi}\dot{t} + g_{\phi\phi}\dot{\phi} = L_z\,. \tag{14}$$

From the two equations above, we can write $\dot{t}$ and $\dot{\phi}$ in terms of E, L_z, and the metric coefficients

$$\dot{t} = \frac{g_{\phi\phi}E + g_{t\phi}L_z}{g_{t\phi}^2 - g_{tt}g_{\phi\phi}}\,, \tag{15}$$

$$\dot{\phi} = -\frac{g_{t\phi}E + g_{tt}L_z}{g_{t\phi}^2 - g_{tt}g_{\phi\phi}}\,. \tag{16}$$

2.2. Infinitesimally Thin Disk

Equations (15) and (16) directly follow from the conservation of E and L_z, and there are no assumptions about the orbits in the spacetime. Now, we want to describe the motion of the material in an accretion disk. This accretion disk is infinitesimally thin and perpendicular to the black hole spin axis, so the motion of the material has $\theta = \pi/2$ and $\dot{\theta} = 0$.

2.3. Motion in the Disk Region ($r > r_{\rm ISCO}$)

The motion of the material in the disk is approximated with *quasi*-geodesic equatorial circular orbits[5], so $\dot{r} = 0$. Let us write the geodesic equations in the following form:

$$\frac{d}{d\tau}\left(g_{\mu\nu}\dot{x}^\nu\right) = \frac{1}{2}\left(\partial_\mu g_{\nu\rho}\right)\dot{x}^\nu\dot{x}^\rho\,. \tag{17}$$

For equatorial circular orbits, $\dot{r} = \ddot{r} = \dot{\theta} = 0$, and for $\mu = r$, Equation (17) reduces to

$$\left(\partial_r g_{tt}\right)\dot{t}^2 + 2\left(\partial_r g_{t\phi}\right)\dot{t}\dot{\phi} + \left(\partial_r g_{\phi\phi}\right)\dot{\phi}^2 = 0\,. \tag{18}$$

The angular velocity of the material as measured by the coordinate system (t, r, θ, ϕ) is $\Omega_{\rm K} = d\phi/dt = \dot{\phi}/\dot{t}$, and the previous equation becomes[6]

$$\begin{aligned} \left(\partial_r g_{\phi\phi}\right)\Omega_{\rm K}^2 + 2\left(\partial_r g_{t\phi}\right)\Omega_{\rm K} + \left(\partial_r g_{tt}\right) &= 0 \\ \Rightarrow \quad \Omega_{\rm K} &= \frac{-\partial_r g_{t\phi} \pm \sqrt{\left(\partial_r g_{t\phi}\right)^2 - \left(\partial_r g_{tt}\right)\left(\partial_r g_{\phi\phi}\right)}}{\partial_r g_{\phi\phi}}\,, \end{aligned} \tag{19}$$

where the sign $+$ is for co-rotating orbits (orbits with angular momentum parallel to the black hole spin) and the sign $-$ is for counter-rotating orbits (orbits with angular momentum anti-parallel to the black hole spin).

Since the material of the disk follows time-like geodesics, which we are parametrizing with the proper time τ, we have $g_{\mu\nu}\dot{x}^\mu\dot{x}^\nu = -1$. Since $\dot{r} = \dot{\theta} = 0$ and $\dot{\phi} = \Omega_{\rm K}\dot{t}$, we have

$$g_{tt}\dot{t}^2 + 2g_{t\phi}\dot{t}\dot{\phi} + g_{\phi\phi}\dot{\phi}^2 = -1 \quad \Rightarrow \quad \dot{t} = \frac{1}{\sqrt{-g_{tt} - 2g_{t\phi}\Omega_{\rm K} - g_{\phi\phi}\Omega_{\rm K}^2}}\,. \tag{20}$$

At this point, we can write the specific energy E and the axial component of the specific angular momentum L_z for geodesic, equatorial, and circular orbits in terms of known quantities

$$E = -\left(g_{tt} + g_{t\phi}\Omega_{\rm K}\right)\dot{t} = -\frac{g_{tt} + g_{t\phi}\Omega_{\rm K}}{\sqrt{-g_{tt} - 2g_{t\phi}\Omega_{\rm K} - g_{\phi\phi}\Omega_{\rm K}^2}}\,, \tag{21}$$

$$L_z = \left(g_{t\phi} + g_{\phi\phi}\Omega_{\rm K}\right)\dot{t} = \frac{g_{t\phi} + g_{\phi\phi}\Omega_{\rm K}}{\sqrt{-g_{tt} - 2g_{t\phi}\Omega_{\rm K} - g_{\phi\phi}\Omega_{\rm K}^2}}\,. \tag{22}$$

Since the motion of the material is determined by the gravitational field of the black hole (and we ignore the pressure of the fluid and possible magnetic fields), the inner edge of the accretion disk can naturally be at the radius of the *innermost stable circular orbit* (ISCO) [34]. Inside the ISCO, circular orbits are unstable, so the material can quickly plunge onto the black hole. To find the ISCO radius, we need to study the stability of the geodesic equatorial circular orbits. From $g_{\mu\nu}\dot{x}^\mu\dot{x}^\nu = -1$ and using Equations (15) and (16), we can write

$$g_{rr}\dot{r}^2 + g_{\theta\theta}\dot{\theta}^2 = V_{\rm eff}(r, \theta)\,, \tag{23}$$

where

$$V_{\rm eff} = \frac{g_{\phi\phi}E^2 + 2g_{t\phi}EL_z + g_{tt}L_z^2}{g_{t\phi}^2 - g_{tt}g_{\phi\phi}} - 1\,. \tag{24}$$

Orbits are stable (unstable) under small perturbations along the radial and vertical directions if, respectively,

$$\frac{\partial^2 V_{\rm eff}}{\partial r^2} < 0 \quad (>0)\,, \qquad \frac{\partial^2 V_{\rm eff}}{\partial \theta^2} < 0 \quad (>0) \tag{25}$$

In the Kerr spacetime and in many other black hole spacetimes, equatorial circular orbits are always stable along the vertical direction, the ISCO radius is determined by the stability along the radial direction, and there is one ISCO radius separating stable orbits ($r > r_{\rm ISCO}$) and unstable orbits ($r < r_{\rm ISCO}$). In general, this is not guaranteed: orbits may be even vertically unstable and/or there may be more than one stable region and/or more than one unstable region [35,36].

2.4. Motion in the Plunging Region ($r_+ < r < r_{\rm ISCO}$)

At $r = r_{\rm ISCO}$, equatorial circular geodesics become unstable. We can approximate the motion of the material in the plunging region ($r_+ < r < r_{\rm ISCO}$, where r_+ is the radial coordinate of the black hole event horizon in the equatorial plane) with equatorial geodesic orbits with specific energy $E^{\rm ISCO}$ and the axial component of the specific angular momentum $L_z^{\rm ISCO}$, where $E^{\rm ISCO}$ and $L_z^{\rm ISCO}$ are E and L_z at $r = r_{\rm ISCO}$.

The 4-velocity of the material in the plunging region is $u^\mu = (\dot{t}, \dot{r}, 0, \dot{\phi})$. $\dot{t}$ and $\dot{\phi}$ are given by Equations (15) and (16) for $E = E^{\rm ISCO}$, $L_z = L_z^{\rm ISCO}$, and $\theta = \pi/2$

$$\dot{t} = \frac{g_{\phi\phi} E^{\rm ISCO} + g_{t\phi} L_z^{\rm ISCO}}{g_{t\phi}^2 - g_{tt} g_{\phi\phi}}, \tag{26}$$

$$\dot{\phi} = -\frac{g_{t\phi} E^{\rm ISCO} + g_{tt} L_z^{\rm ISCO}}{g_{t\phi}^2 - g_{tt} g_{\phi\phi}}. \tag{27}$$

$\dot{r}$ can be inferred from $g_{\mu\nu} \dot{x}^\mu \dot{x}^\nu = -1$

$$\begin{aligned} \dot{r} &= -\sqrt{\frac{-1 - g_{tt}\dot{t}^2 - 2 g_{t\phi}\dot{t}\dot{\phi} - g_{\phi\phi}\dot{\phi}^2}{g_{rr}}} \\ &= -\sqrt{\frac{1}{g_{rr}} \left[\frac{g_{\phi\phi} (E^{\rm ISCO})^2 + 2 g_{t\phi} E^{\rm ISCO} L_z^{\rm ISCO} + g_{tt} (L_z^{\rm ISCO})^2}{g_{t\phi}^2 - g_{tt} g_{\phi\phi}} - 1 \right]}, \end{aligned} \tag{28}$$

where the sign $-$ in front of the square root is chosen because the material is falling onto the black hole. It can be useful to stress that $\dot{t}$, $\dot{\phi}$, and $\dot{r}$ are functions only of the radial coordinate r, so we have the 4-velocity of the accreting material in the plunging region at every radial coordinate.

The presence of magnetic fields can make the model significantly more complicated. General Relativistic Magnetohydrodynamic (GRMHD) simulations can provide the most reliable description of the accretion process onto compact objects, even if current simulations still rely on a number of simplifications, so caution is necessary when we want to derive conclusions for the accretion process on astrophysical black holes, and the morphology of magnetic fields around black holes is still poorly understood. Current GRMHD studies suggest that thin accretion disks are close to being Keplerian, and the simple model described in Section 2.3 can well approximate the motion of the material in the disk region [37]. Magnetic fields can instead affect the motion of the material in the plunging region and change the location of the inner edge of the disk, which may not be $r_{\rm ISCO}$ any longer. In such a case, Equations (26)–(28) may not well describe the motion in the plunging region. The simplest models to describe the motion of the material in the plunging region in the presence of magnetic fields still assume that the motion is on the equatorial plane ($\theta = \pi/2$ and $\dot{\theta} = 0$) and consider simple modifications in the Lagrangian in Equation (12) to slow down the fall of the material from the ISCO to the black hole.

3. Corona

This section is devoted to studying how the corona illuminates the accretion disk.

3.1. Coronal Spectrum

We start assuming that the corona is a point-like source. An extended corona can be easily described as the combination of a number of point-like coronae.

The *photon spectrum* of the corona in its rest-frame can be approximated by a power law with a high-energy cutoff $E_{\rm max}$ and a low-energy cutoff $E_{\rm min}$ [5], so we can write

$$\frac{dN_{\rm c}}{dt_{\rm c} dE_{\rm c}} = \begin{cases} K E_{\rm c}^{-\Gamma} & E_{\rm min} < E_{\rm c} < E_{\rm max} \\ 0 & \text{otherwise} \end{cases}, \tag{29}$$

where $N_{\rm c}$ is the photon number, K is a normalization constant, Γ is the photon index, and the subindex c indicates that a quantity is evaluated in the rest-frame of the corona. The spectral luminosity of the corona is

$$\frac{dL_{\rm c}}{dE_{\rm c}} = E_{\rm c}\frac{dN_{\rm c}}{dt_{\rm c}dE_{\rm c}}\,, \tag{30}$$

and the total luminosity of the corona is

$$L_{\rm c} = \int E_{\rm c}\frac{dN_{\rm c}}{dt_{\rm c}dE_{\rm c}}\,dE_{\rm c} = \int_{E_{\rm min}}^{E_{\rm max}} KE_{\rm c}^{-\Gamma+1}\,dE_{\rm c} = \begin{cases} \frac{K}{2-\Gamma}\left[E_{\rm max}^{2-\Gamma} - E_{\rm min}^{2-\Gamma}\right] & \Gamma \neq 2 \\ K\ln\left(\frac{E_{\rm max}}{E_{\rm min}}\right) & \Gamma = 2 \end{cases}. \tag{31}$$

If we know the total luminosity of the corona and its spectrum, we can fix the normalization constant K.

The spectrum of the corona detected far from the source is not exactly that in Equation (29) because it is redshifted. The redshift factor is

$$g = \frac{E_{\rm o}}{E_{\rm c}} = \frac{-u_{\rm o}^{\mu}k_{\mu}}{-u_{\rm c}^{\mu}k_{\mu}}\,, \tag{32}$$

where $u_{\rm o}^{\mu} = (1,0,0,0)$ is the 4-velocity of the distant observer, $u_{\rm c}^{\mu}$ is the 4-velocity of the point-like corona, and $k_{\mu} = (k_t, k_r, k_\theta, k_\phi)$ is the conjugate 4-momentum of the photons emitted by the corona and detected by the distant observer. k_{μ} should be evaluated at the detection point in the numerator and at the corona in the denominator. The photon spectrum of the corona detected by the distant observer is

$$\frac{dN_{\rm o}}{dt_{\rm o}dE_{\rm o}} = \begin{cases} K'E_{\rm o}^{-\Gamma} & E'_{\rm min} < E_{\rm o} < E'_{\rm max} \\ 0 & \text{otherwise} \end{cases}\,, \tag{33}$$

where $E'_{\rm max} = gE_{\rm max}$ and $E'_{\rm min} = gE_{\rm min}$ are, respectively, the redshifted high-energy cutoff and the redshifted low-energy cutoff, $K' = g^{\Gamma}K$, and the subindex o indicates that a quantity is evaluated in the rest-frame of the observer. The photon number is an invariant. If the corona emits photons from time $t_{\rm c}$ to time $t_{\rm c} + \Delta t_{\rm c}$ in the corona rest-frame, the total number of photons is (for $\Gamma \neq 1$)

$$N_{\rm c} = \int_{t_{\rm c}}^{t_{\rm c}+\Delta t_{\rm c}} dt_{\rm c}\int_{E_{\rm min}}^{E_{\rm max}} dE_{\rm c}\,KE_{\rm c}^{-\Gamma} = \frac{\Delta t_{\rm c}K}{1-\Gamma}\left[E_{\rm max}^{1-\Gamma} - E_{\rm min}^{1-\Gamma}\right]. \tag{34}$$

The total number of photons detected by the distant observer is

$$\begin{aligned} N_{\rm o} &= \int_{t_{\rm o}}^{t_{\rm o}+\Delta t_{\rm o}} dt_{\rm o}\int_{E'_{\rm min}}^{E'_{\rm max}} dE_{\rm o}\,K'E_{\rm o}^{-\Gamma} = \frac{\Delta t_{\rm o}K'}{1-\Gamma}\left[E'^{1-\Gamma}_{\rm max} - E'^{1-\Gamma}_{\rm min}\right] \\ &= \frac{\left(g^{-1}\Delta t_{\rm c}\right)\left(g^{\Gamma}K\right)}{1-\Gamma}\left[\left(g^{1-\Gamma}\right)E_{\rm max}^{1-\Gamma} - \left(g^{1-\Gamma}\right)E_{\rm min}^{1-\Gamma}\right] = N_{\rm c}\,. \end{aligned} \tag{35}$$

3.2. Illumination of the Accretion Disk

To calculate how the corona illuminates the disk, we fire $\mathcal{N}$ photons from the corona to the disk, where $\mathcal{N}$ is a sufficiently large number to meet our requirements of accuracy for the final result. If the corona emission is isotropic in its rest-frame, we consider the rest-frame of the corona, and we isotropically fire these $\mathcal{N}$ photons. If this is not the case, we consider the rest-frame of the corona, and we fire $\mathcal{N}$ photons according to the specific angular emission law of the corona such that any photon trajectory can represent the same

number of photons per unit time and unit energy. The photon spectrum for every emission direction (ray) is

$$\frac{dN_{\rm c}}{dt_{\rm c}dE_{\rm c}} = \begin{cases} \tilde{K}E_{\rm c}^{-\Gamma} & E_{\rm min} < E < E_{\rm max} \\ 0 & \text{otherwise} \end{cases}, \tag{36}$$

where $\tilde{K} = K/\mathcal{N}$.

As an example, let us assume that the corona is an infinitesimally thin disk above the accretion disk and the black hole as shown in Figure 3 [38]. The system is perfectly axisymmetric, so the central axis of the corona coincides with that of the accretion disk and with the rotational axis of the black hole. The corona may rotate with angular frequency $\tilde{\omega}$ as measured in the spherical-like coordinates (t, r, θ, ϕ). Since the system is axisymmetric, we can restrict our calculations to a certain radial direction. We consider a number of point-like coronae along such a radial direction and, as shown in Figure 3, we indicate with R the radial coordinate of every point-like corona from the central axis. The spacing of the point-like coronae can be used to regulate the intensity profile of our disk-like corona. For example, if we assume that the surface of the corona has constant luminosity, we need a point-like corona for every equal-area annulus. In the Newtonian limit, the area of the annulus of radius R and width ΔR is $2\pi R \Delta R$, and therefore we would need to distribute the point-like coronae with a separation $\Delta R \propto 1/R$. If we employ $\Delta R =$ constant, it is equivalent to assume that the intensity profile of the corona scales as $1/R$.

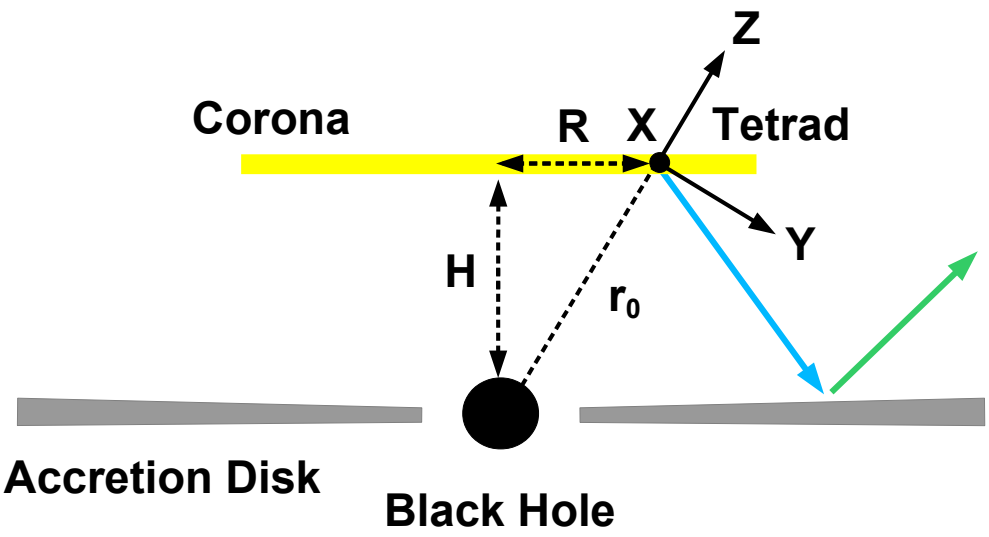

Figure 3. Rotating disk-like corona: an extended corona can be thought of as the combination of a number of point-like coronae. For every point-like corona, we consider its locally Minkowskian reference frame, and we fire $\mathcal{N}$ photons. We calculate the null geodesics from the point-like corona to the accretion disk in order to calculate how the point-like corona illuminates the disk. See the text for more details. Figure from Ref. [16].

To write the photon initial conditions, it is convenient to choose the locally Minkowskian reference frames of the point-like coronae (see Appendix A). If u_j^μ is the 4-velocity of the point-like corona j, $u_j^r = u_j^\theta = 0$ (because the corona rotates about the black hole spin axis) and $u_j^\phi = \tilde{\omega} u_j^t$ by definition. From $g_{\mu\nu} u_j^\mu u_j^\nu = -1$, we find u_j^t

$$u_j^t = \frac{1}{\sqrt{-g_{tt} - 2\tilde{\omega} g_{t\phi} - \tilde{\omega}^2 g_{\phi\phi}}}. \tag{37}$$

The time-like tetrad basis vector $E^\mu_{(T)}$ is u^μ_j. We choose the orientation of the space-like tetrad basis vectors as shown in Figure 3 with $\hat{r} = \hat{Z}$ and $\hat{\theta} = \hat{Y}$. The expression for $E^\mu_{(X)}$ can be inferred from the conditions $g_{\mu\nu}E^\mu_{(X)}E^\nu_{(X)} = 1$ and $g_{\mu\nu}E^\mu_{(X)}E^\nu_{(T)} = g_{\mu\nu}E^\mu_{(X)}E^\nu_{(Y)} = g_{\mu\nu}E^\mu_{(X)}E^\nu_{(Z)} = 0$. In the end, the tetrad of the orthogonal basis vectors associated to the locally Minkowskian reference frame of the point-like corona j has the following form:

$$E^\mu_{(T)} = u^t_j \begin{pmatrix} 1 \\ 0 \\ 0 \\ \tilde{\omega} \end{pmatrix}, \quad E^\mu_{(X)} = \frac{u^t_j}{\sqrt{g^2_{t\phi} - g_{tt}g_{\phi\phi}}} \begin{pmatrix} g_{t\phi} + \tilde{\omega}g_{\phi\phi} \\ 0 \\ 0 \\ -g_{tt} - \tilde{\omega}g_{t\phi} \end{pmatrix},$$
$$E^\mu_{(Y)} = \frac{1}{\sqrt{g_{\theta\theta}}} \begin{pmatrix} 0 \\ 0 \\ 1 \\ 0 \end{pmatrix}, \quad E^\mu_{(Z)} = \frac{1}{\sqrt{g_{rr}}} \begin{pmatrix} 0 \\ 1 \\ 0 \\ 0 \end{pmatrix}. \tag{38}$$

For every point-like corona, we fire $\mathcal{N}$ photons and check if and where these photons hit the accretion disk. In the locally Minkowskian reference frame of the point-like corona, the initial 4-momentum of the photons can be written as

$$k^{(\alpha)}_0 = \begin{pmatrix} E \\ E\sin\chi\cos\psi \\ E\sin\chi\sin\psi \\ E\cos\chi \end{pmatrix}, \tag{39}$$

where E is the photon energy, and $\chi \in [0;\pi]$ and $\psi \in [0;2\pi]$ are the polar angles in the locally Minkowskian reference frame of the point-like corona. If the emission of the point-like corona is isotropic, we can consider a grid of constant $\Delta(\cos\chi)$ and $\Delta\psi$, and fire a photon from every point of the grid[7]. In the spherical-like coordinates (t, r, θ, ϕ), the initial conditions for the photon position will be like

$$t_0 = 0\,, \quad r_0 = \sqrt{H^2 + R^2}\,, \quad \theta_0 = \arctan\left(\frac{R}{H}\right), \quad \phi_0 = 0\,. \tag{40}$$

The initial conditions for the photon 4-momentum will be like

$$k^\mu_0 = k^{(\alpha)}_0 E^\mu_{(\alpha)}\,. \tag{41}$$

In our case, with the tetrad in (38), we have

$$k^t_0 = k^{(T)}_0 E^t_{(T)} + k^{(X)}_0 E^t_{(X)}\,, \quad k^r_0 = k^{(Z)}_0 E^r_{(Z)}\,, \quad k^\theta_0 = k^{(Y)}_0 E^\theta_{(Y)}\,,$$
$$k^\phi_0 = k^{(T)}_0 E^\phi_{(T)} + k^{(X)}_0 E^\phi_{(X)}\,. \tag{42}$$

With the initial conditions in (40) and (42), we solve the geodesic equations in the coordinate system (t, r, θ, ϕ). We calculate the trajectory of every photon of the grid of the point-like corona, and then we repeat these calculations for every point-like corona.

3.3. Spectral Flux Illuminating the Disk

We divide the accretion disk into annuli (radial bins). The annulus i has radial coordinate r_i and width Δr_i. We fire photons from the point-like corona j to the disk as discussed in the previous subsection. If the ray k ($k = 1, \ldots, \mathcal{N}$) hits the annulus i, it deposits the following energy on the annulus i with photons of energy E_d

$$d\varepsilon_{ijk} = E_\mathrm{d} dN\,, \tag{43}$$

where dN is the photon number, which is conserved along the photon path because we are in vacuum and there is no photon emission or absorption. The photon number of a ray in the rest-frame of the corona is

$$dN = \tilde{K} E_{\rm c}^{-\Gamma}\, dt_{\rm c}\, dE_{\rm c}\,, \tag{44}$$

The redshift factor between the emission point (the point-like corona j) and the incident point (the annulus i) of the ray k is

$$g_{ijk} = \frac{E_{\rm d}}{E_{\rm c}} = \frac{-u_i^\mu k_\mu}{-u_j^\mu k_\mu} = \left[\frac{1 - b_k\,\Omega_{\rm K}}{\sqrt{-g_{tt} - 2\Omega_{\rm K} g_{t\phi} - \Omega_{\rm K}^2 g_{\phi\phi}}}\right]_i \left[\frac{\sqrt{-g_{tt} - 2\tilde{\omega} g_{t\phi} - \tilde{\omega}^2 g_{\phi\phi}}}{1 - b_k\,\tilde{\omega}}\right]_j\,, \tag{45}$$

where $b_k = -k_\phi/k_t$ is a constant of motion of the ray k, the subindices i and j in the last expression are used to indicate that the first term is evaluated at the annulus i and the second term is evaluated at the point-like corona j, $\Omega_{\rm K}$ is the angular velocity of the material in the disk given in Equation (19), and $\tilde{\omega}$ is the angular velocity of the point-like corona. We can thus rewrite Equation (44) as

$$dN = \tilde{K}\, g_{ijk}^\Gamma\, E_{\rm d}^{-\Gamma}\, dt_{\rm d}\, dE_{\rm d}\,. \tag{46}$$

The spectral flux on the annulus i produced by the ray k of the point-like corona j is

$$F_{{\rm X},ijk} = \frac{d\varepsilon_{ijk}}{d\sigma_i\, dt_{\rm d}\, dE_{\rm d}} = \frac{\tilde{K}\, g_{ijk}^\Gamma\, E_{\rm d}^{-\Gamma+1}}{A_i}\,, \tag{47}$$

where A_i is the *proper area* of the annulus i (see Appendix B)

$$A(r_i, \Delta r_i) = 2\pi \Delta r_i \left[\sqrt{\frac{g_{rr}\left(g_{t\phi}^2 - g_{tt} g_{\phi\phi}\right)}{-g_{tt} - 2 g_{t\phi}\Omega_{\rm K} - g_{\phi\phi}\Omega_{\rm K}^2}}\right]_{r=r_i,\theta=\pi/2}\,. \tag{48}$$

If the ray k hits the plunging region and we want to include the emission of the plunging region in the calculations, we proceed in the same way, but we need to use the 4-velocity of the material in the plunging region for u_i^μ (see Section 2.4) and the proper area of an annulus in the plunging region for $A(r_i, \Delta r_i)$[8].

The spectral flux on the annulus i produced by the disk-like corona is obtained by summing over all rays for every point-like corona and then over all point-like coronae

$$F_{{\rm X},i} = \sum_j \sum_k F_{{\rm X},ijk}\,. \tag{49}$$

The total flux illuminating the annulus i by the disk-like corona is

$$F_i = \int F_{{\rm X},i}\, dE_{\rm d}\,. \tag{50}$$

Note that the ionization parameter of the annulus i is

$$\xi_i = \frac{4\pi F_i}{n_{{\rm e},i}}\,, \tag{51}$$

where $n_{{\rm e},i}$ is the electron density of the annulus i.

We repeat these calculation for every annulus i of the accretion disk and we find the spectral flux and the total flux at every radial coordinate: $F_{\rm X} = F_{\rm X}(r)$ and $F = F(r)$.

If we are interested only in the X-ray flux illuminating the disk (0.1–100 keV) and $g_{ijk} E_{\rm min} < 0.1$ keV and $g_{ijk} E_{\rm max} > 100$ keV, Equations (49) and (50) become, respectively, (for $\Gamma \neq 2$)

$$F_{{\rm X},i}(E_{\rm d}) = \frac{\tilde{K}\, E_{\rm d}^{-\Gamma+1}}{A_i} \sum_j \sum_k g_{ijk}^{\Gamma}\,, \tag{52}$$

$$F_i = \frac{\tilde{K}}{A_i (2-\Gamma)} \left[E_{\rm high}^{2-\Gamma} - E_{\rm low}^{2-\Gamma} \right] \sum_j \sum_k g_{ijk}^{\Gamma}\,, \tag{53}$$

where $E_{\rm low} = 0.1$ keV and $E_{\rm high} = 100$ keV.

If the photon index Γ changes over the corona, Equation (44) becomes

$$dN = \tilde{K} E_{\rm c}^{-\Gamma_j}\, dt_{\rm c}\, dE_{\rm c}\,, \tag{54}$$

where Γ_j is the photon index of the point-like corona j. We can proceed in the same way, and the spectral flux and the total flux of the disk-like corona will be still given by Equations (49) and (50).

If the corona moves at mildly relativistic velocities with respect to the disk, relativistic effects may significantly alter the illumination of the disk [39,40] and therefore the motion of the corona should be included in the calculations.

4. Non-Relativistic Reflection Spectrum

The *non-relativistic* reflection spectrum is the reflection spectrum in the rest-frame of the material of the disk. In the previous section, we calculated the spectrum of the radiation illuminating the disk. We can plug this spectrum in a reflection model (like `reflionx` [18] or `xillver` [17]) and obtain as the output the non-relativistic reflection spectrum.

In general relativity, the atomic physics near a black hole is the same as the atomic physics in our laboratories on Earth. This is because in general relativity, the gravitational interaction is only described by the metric tensor $g_{\mu\nu}$, and locally the laws of non-gravitational physics are those of Special Relativity: indeed, we can always perform a coordinate transformation and find a locally inertial reference frame (see, for example, Subsection 6.4.2 in Ref. [41]). In theories beyond general relativity, this may not be true[9].

If we know the spectrum of the radiation at every radius of the accretion disk, we can calculate the non-relativistic reflection spectrum at every radial coordinate. Since this tutorial is focused on the relativistic calculations, and the calculations of non-relativistic reflection spectra involve only atomic physics (at least in general relativity and in any other metric theory of gravity), here we briefly present the main results and the reader can find more details in [17,18] and the references therein. In general, the calculation of a non-relativistic reflection spectrum requires solving some radiative transfer equations. Figures 4–6 show non-relativistic reflection spectra calculated by the `xillver` model [17][10] assuming that the incident radiation is described by a power law with photon index Γ and high-energy cutoff $E_{\rm cut} = 300$ keV, and illuminates a cold material with incident angle $\vartheta_{\rm i} = 45^\circ$ (i.e., the angle between the propagation direction of the incident photons and the normal to the surface of the cold material in the rest-frame of the cold material). The cold material is characterized by the electron density N, the ionization parameter ξ (defined as in Equation (51)), and has solar elemental abundances. The emission angle is $\vartheta_{\rm e} = 60^\circ$ (i.e., the angle between the propagation direction of the emitted photons and the normal to the surface of the cold material in the rest-frame of the cold material). Figure 4 shows how a non-relativistic reflection spectrum changes if we change the value of the photon index Γ of the incident radiation, while Figures 5 and 6 show, respectively, the impact of the ionization parameter and of the electron density.

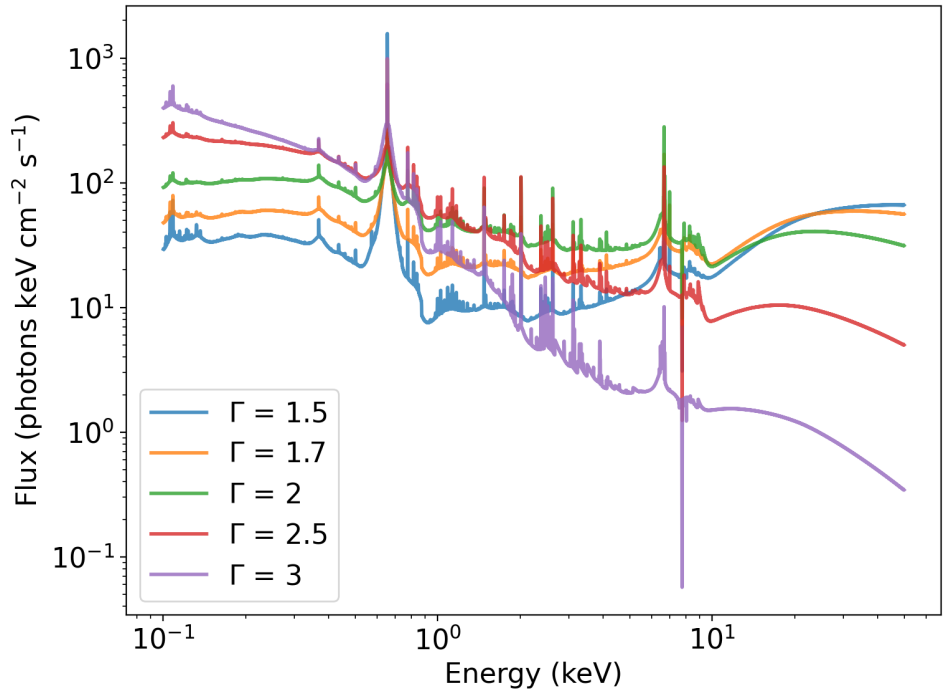

Figure 4. Examples of non-relativistic reflection spectra produced with `xillver` [17] for different values of the photon index Γ and assuming that the high-energy cutoff is $E_{\rm cut} = 300$ keV, the incident angle is $\vartheta_{\rm i} = 45^\circ$, the emission angle is $\vartheta_{\rm e} = 60^\circ$, the ionization parameter is $\log \xi = 3$ (ξ in units of erg cm s^{-1}), and the electron density is $\log N = 18$ (N in units of cm^{-3}).

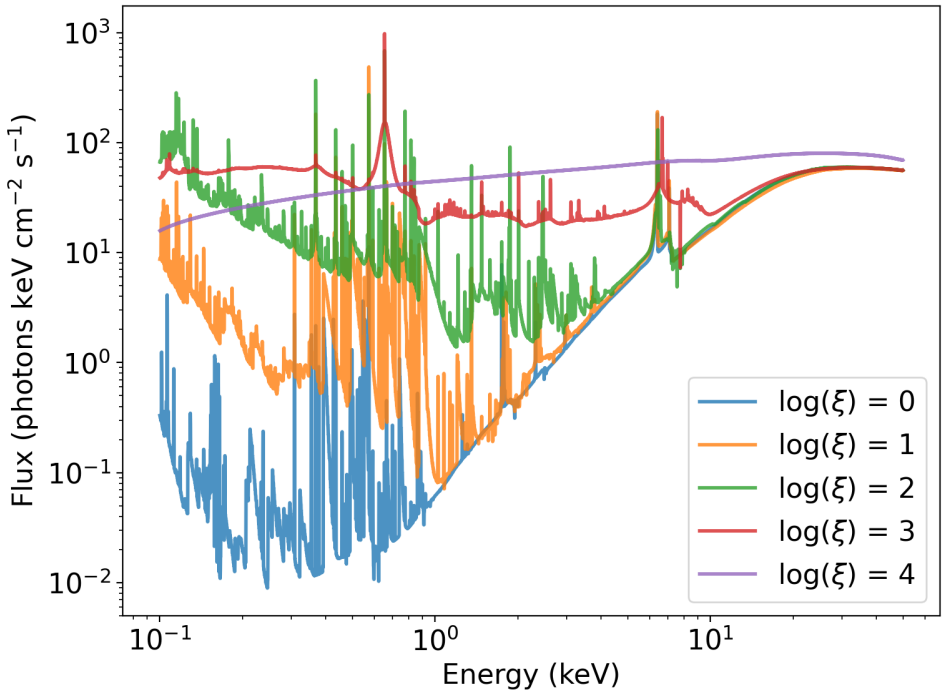

Figure 5. As in Figure 4 for Γ = 1.7 and different values of the ionization parameter ξ (ξ in units of erg cm s^{-1}).

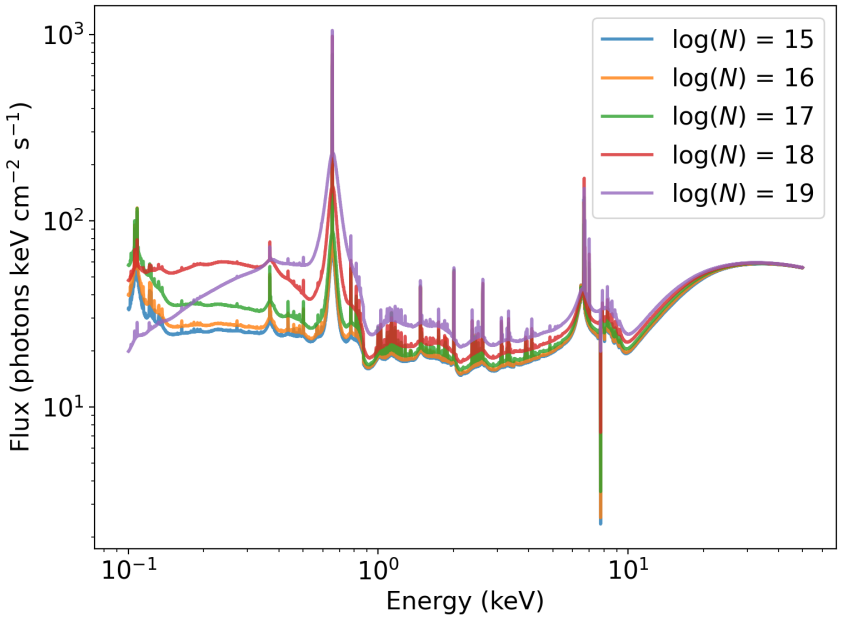

Figure 6. As in Figure 4 for $\Gamma = 1.7$ and different values of the electron density N (N in units of cm^{-3}).

5. Returning Radiation

The *returning radiation* (or self-irradiation) is the radiation emitted by the disk and returning to the disk because of the phenomenon of light bending. Figure 7 shows the fractions of photons that at every emission radius return to the disk (red curve), fall onto the black hole or the plunging region (black curve), or escape to infinity (blue curve). The plot refers to the case of an infinitesimally thin Keplerian disk in the equatorial plane of a Kerr black hole with spin parameter $a_* = 0.998$. As we can see from Figure 7, the fraction of photons returning to the accretion disk is relevant only at very small radii, say, $r < 2\,M$, while at larger radii, most of the radiation can escape to infinity [43].

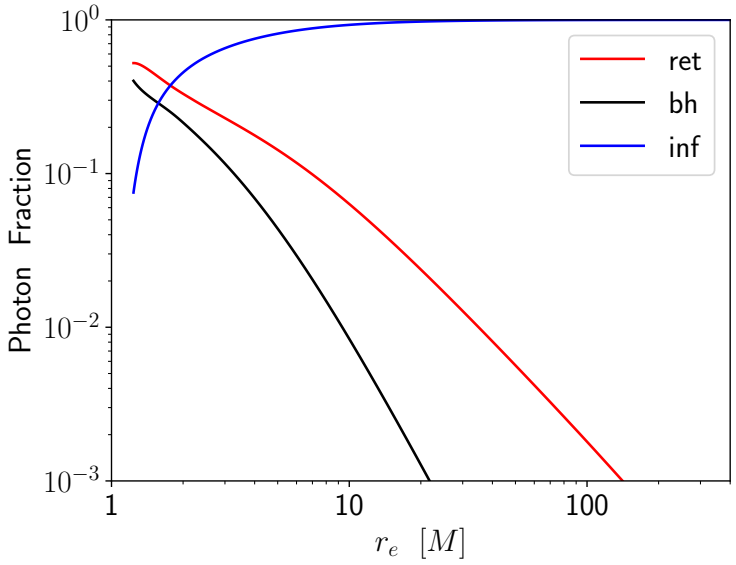

Figure 7. Fraction of photons that at every emission radius $r_{\rm e}$ return to the accretion disk (returning radiation, red curve), fall onto the black hole or the plunging region (black curve), or escape to infinity (blue curves). We assume that the compact object is a Kerr black hole with spin parameter $a_* = 0.998$ and that the accretion disk is Keplerian, infinitesimally thin, and perpendicular to the black hole spin axis. We ignore the radiation from the plunging region, and the three curves start from $r_{\rm e} = r_{\rm ISCO}$ on the left. Figure from Ref. [16].

To include the returning radiation in our calculations, we can consider a number of points on the accretion disk along a certain radial direction and fire photons from every point to study if and where they return to the accretion disk. At every emission point, we consider the locally Minkowskian reference frame associated to the material of the accretion disk. In the disk region $r > r_{\rm ISCO}$, the tetrad of the orthogonal basis vectors and its inverse are those reported in Equations (A6) and (A7) with $\omega = \Omega_{\rm K}$

$$
\begin{aligned}
E^\mu_{(T)} &= u^t \begin{pmatrix} 1 \\ 0 \\ 0 \\ \Omega_{\rm K} \end{pmatrix}, \; E^\mu_{(X)} = \frac{1}{\sqrt{g_{rr}}} \begin{pmatrix} 0 \\ 1 \\ 0 \\ 0 \end{pmatrix}, \\
E^\mu_{(Y)} &= \frac{u^t}{\sqrt{g_{t\phi}^2 - g_{tt} g_{\phi\phi}}} \begin{pmatrix} g_{t\phi} + \Omega_{\rm K} g_{\phi\phi} \\ 0 \\ 0 \\ -g_{tt} - \Omega_{\rm K} g_{t\phi} \end{pmatrix}, \; E^\mu_{(Z)} = \frac{1}{\sqrt{g_{\theta\theta}}} \begin{pmatrix} 0 \\ 0 \\ 1 \\ 0 \end{pmatrix}, \qquad (55) \\
E^{(T)}_\mu &= -u^t \begin{pmatrix} g_{tt} + \Omega_{\rm K} g_{t\phi} \\ 0 \\ 0 \\ g_{t\phi} + \Omega_{\rm K} g_{\phi\phi} \end{pmatrix}, \; E^{(X)}_\mu = \sqrt{g_{rr}} \begin{pmatrix} 0 \\ 1 \\ 0 \\ 0 \end{pmatrix}, \\
E^{(Y)}_\mu &= u^t \sqrt{g_{t\phi}^2 - g_{tt} g_{\phi\phi}} \begin{pmatrix} -\Omega_{\rm K} \\ 0 \\ 0 \\ 1 \end{pmatrix}, \; E^{(Z)}_\mu = \sqrt{g_{\theta\theta}} \begin{pmatrix} 0 \\ 0 \\ 1 \\ 0 \end{pmatrix}, \qquad (56)
\end{aligned}
$$

and u^t is given in Equation (20) because we are considering the material in the disk.

In the plunging region $r_+ < r < r_{\rm ISCO}$, $E^\mu_{(T)} = (u^t, u^r, 0, u^\phi)$, where u^t, u^r, and u^ϕ are given, respectively, by Equations (26) and (27). $E^\mu_{(Z)} = (0, 0, 1/\sqrt{g_{\theta\theta}}, 0)$ as in the disk region because the material is still assumed to be confined on the equatorial plane. $E^\mu_{(X)}$ and $E^\mu_{(Y)}$ can be found from the condition $g_{\mu\nu} E^\mu_{(\alpha)} E^\nu_{(\beta)} = \eta_{(\alpha)(\beta)}$.

In such locally Minkowskian reference frames, the 4-momentum of the photons have the form

$$
k_0^{(\alpha)} = \begin{pmatrix} k_0^{(T)} \\ k_0^{(X)} \\ k_0^{(Y)} \\ k_0^{(Z)} \end{pmatrix} = \begin{pmatrix} E \\ E \sin\vartheta_{\rm e} \cos\varphi_{\rm e} \\ E \sin\vartheta_{\rm e} \sin\varphi_{\rm e} \\ E \cos\vartheta_{\rm e} \end{pmatrix}, \qquad (57)
$$

where E is the photon energy, and $\vartheta_{\rm e} \in [0; \pi/2]$ and $\varphi_{\rm e} \in [0; 2\pi]$ are the polar angles in the rest-frame of the material of the disk. If the emission is isotropic, we can consider a grid of constant $\Delta(\cos\vartheta_{\rm e})$ and $\Delta\varphi_{\rm e}$ and fire a photon from every point of the grid. The photon 4-momenta in the coordinate system (t, r, θ, ϕ) can be obtained from

$$
k_0^\mu = E^\mu_{(\alpha)} k_0^{(\alpha)} \,. \qquad (58)
$$

We can then solve the geodesic equations in the coordinate system (t, r, θ, ϕ) to calculate the photon trajectories and study which trajectories return to the disk. For the photons that return to the disk, we can calculate the redshift factor

$$
g = \frac{E_2}{E_1} = \frac{-u_2^\mu k_\mu}{-u_1^\mu k_\mu} \qquad (59)
$$

where the subindices 1 and 2 refer, respectively, to the emission point and the absorption point. In the numerator, we have the 4-velocity of the material in the disk and the photon

4-momentum at the absorption point. In the denominator, we have the 4-velocity of the material in the disk and the photon 4-momentum at the emission point. For $r \geq r_{\rm ISCO}$, we use the 4-velocity of the material in the disk region (Section 2.3)

$$u^\mu k_\mu = \frac{1 - b\,\Omega_{\rm K}}{\sqrt{-g_{tt} - 2g_{t\phi}\Omega_{\rm K} - g_{\phi\phi}\Omega_{\rm K}^2}}\,, \tag{60}$$

where $b = -k_\phi/k_t$. For $r < r_{\rm ISCO}$, we use the 4-velocity of the material in the plunging region (Section 2.4)

$$\begin{aligned} u^\mu k_\mu \;=\; & k_t \frac{g_{\phi\phi} E^{\rm ISCO} + g_{t\phi} L_z^{\rm ISCO}}{g_{t\phi}^2 - g_{tt} g_{\phi\phi}} - k_\phi \frac{g_{t\phi} E^{\rm ISCO} + g_{tt} L_z^{\rm ISCO}}{g_{t\phi}^2 - g_{tt} g_{\phi\phi}} \\ & - k_r \sqrt{\frac{1}{g_{rr}} \left[\frac{g_{\phi\phi} (E^{\rm ISCO})^2 + 2 g_{t\phi} E^{\rm ISCO} L_z^{\rm ISCO} + g_{tt} (L_z^{\rm ISCO})^2}{g_{t\phi}^2 - g_{tt} g_{\phi\phi}} - 1 \right]}\,. \end{aligned} \tag{61}$$

We can proceed as in the case of the illumination of the disk by the corona discussed in Section 3. We divide the disk into annuli and we calculate the spectral flux for every annulus as in Equation (49). Note that the total spectral flux illuminating the disk eventually will be the sum of the direct radiation from the corona, the returning radiation of the thermal component of the disk, and the returning radiation of the reflection component [44].

6. Relativistic Reflection Spectrum

Once we have the non-relativistic reflection spectrum at every radial coordinate of the accretion disk, we can proceed to calculate the *relativistic* reflection spectrum, namely, the reflection spectrum of the whole disk as seen by an observer far from the source [21,22]. The observed spectral flux is

$$F_{\rm o}(E_{\rm o}) = \int_{\rm source} I_{\rm o}(E_{\rm o}, X, Y)\, d\Omega = \frac{1}{D^2} \int_{\rm source} g^3\, I_{\rm e}(E_{\rm e}, r_{\rm e}, \vartheta_{\rm e})\, dX dY \tag{62}$$

where the subindices o and e are used to indicate quantities measured in the rest-frame of the distant observer and in the rest-frame of the emitter, respectively. $d\Omega = dXdY/D^2$ is the infinitesimal solid angle in the sky of the distant observer, X and Y are the Cartesian coordinates in the plane of the distant observer[11], and D is the distance between the observer and the source. $g = E_{\rm o}/E_{\rm e}$ is the redshift factor, and $I_{\rm o} = g^3 I_{\rm e}$ follows from Liouville's theorem (see Section 1.2). $r_{\rm e}$ is the emission radius in the accretion disk, and $\vartheta_{\rm e}$ is the emission angle in the rest-frame of the material of the disk, namely, the angle between the normal to the disk and the photon emission direction measured in the rest-frame of the material (which is different, in general, from the inclination angle of the disk i, namely, the angle between the normal to the disk and the line of sight of the distant observer, because of the phenomenon of light bending). The plane of the distant observer is assumed to be perpendicular to the straight line connecting the source and the observer, so the angle θ in the definition of the specific intensity (see Section 1.1) is 0 and $\cos\theta = 1$.

We consider a grid in the image plane of the distant observer. From every point of the grid, we fire a photon and we calculate its trajectory backwards in time from the detection point on the image plane of the distant observer to the emission point on the accretion disk. When the photon hits the disk, say, at the radial coordinate $r_{\rm e}$, we calculate the redshift factor g and the emission angle $\vartheta_{\rm e}$. At this point, for every pixel with Cartesian coordinates (X, Y) and area $dXdY$ of the image of the disk on the plane of the distant observer[12], we have g and $I_{\rm e}$, so we can calculate the integral in Equation (62) and determine the observed flux density. The next subsections present the calculations of the photon initial conditions, redshift factor g, and emission angle $\vartheta_{\rm e}$.

6.1. Photon Initial Conditions

To write the photon initial conditions, we consider the system sketched in Figure 8. We have a black hole, an accretion disk on the equatorial plane of the black hole perpendicular to the black hole spin axis, and an observer far from the black hole. D is the distance between the black hole and the observer, and i is the inclination angle of the disk, namely, the angle between the black hole spin axis and the line of sight of the distant observer. The Cartesian coordinates (x, y, z) are centered at the black hole as shown in Figure 8, so the xy-plane coincides with the plane of the accretion disk, and the z-axis coincides with the black hole spin axis. The distant observer has the Cartesian coordinates (X, Y, Z), where the XY-plane coincides with the image plane of the observer, and the Z-axis coincides with the straight line connecting the black hole and the observer. The Cartesian coordinates (x, y, z) are related to the Cartesian coordinates (X, Y, Z) by the following relations:

$$\begin{aligned} x &= D\sin i - Y\cos i + Z\sin i\,, \\ y &= X\,, \\ z &= D\cos i + Y\sin i + Z\cos i\,. \end{aligned} \tag{63}$$

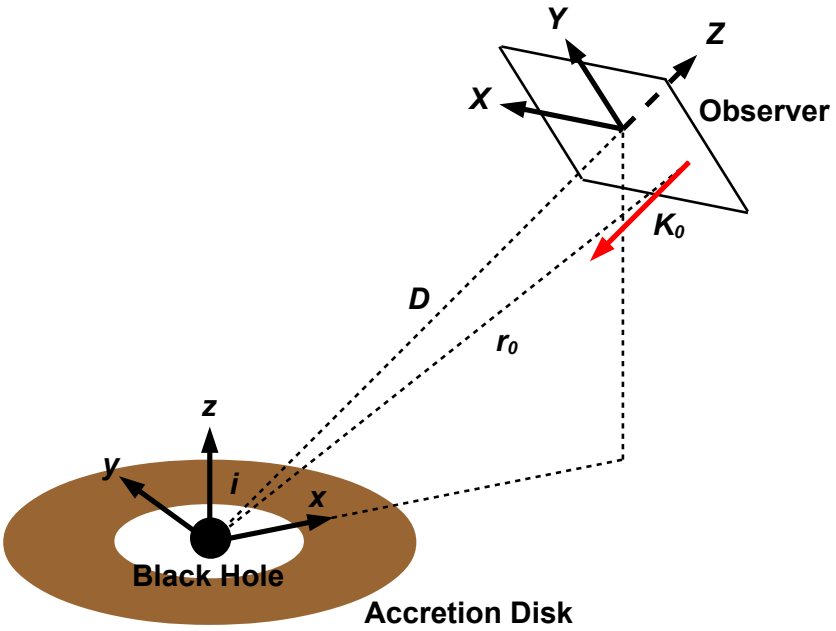

Figure 8. The Cartesian coordinates (x, y, z) are centered at the black hole. The Cartesian coordinates (X, Y, Z) are the coordinate system of the distant observer. D is the distance between the black hole and the distant observer. i is the inclination angle between the black hole spin axis and the line of sight of the distant observer. $\mathbf{K}_0 = (0, 0, -K_0)$ is the initial 3-momentum of a photon in the coordinate system of the distant observer. See the text for more details. Figure from Ref. [16].

The metric of our spacetime is in spherical-like coordinates (t, r, θ, ϕ). Far from the black holes, the spatial coordinates (r, θ, ϕ) reduce to the usual spherical coordinates in flat spacetime and are related to (x, y, z) by

$$\begin{aligned} r &= \sqrt{x^2 + y^2 + z^2}\,, \\ \theta &= \arccos\left(\frac{z}{r}\right), \\ \phi &= \arctan\left(\frac{y}{x}\right). \end{aligned} \tag{64}$$

For the distant observer, a generic photon has the initial position of the form $(X_0, Y_0, 0)$ and initial 3-momentum of the form $\mathbf{K}_0 = (0, 0, -K_0)$ because the photon trajectory is

perpendicular to the XY-plane. In the coordinate system (t, r, θ, ϕ), the initial position of the photon is

$$\begin{aligned} t_0 &= 0\,, \\ r_0 &= \sqrt{X_0^2 + Y_0^2 + D^2}\,, \\ \theta_0 &= \arccos\left(\frac{Y_0 \sin i + D \cos i}{r_0}\right), \\ \phi_0 &= \arctan\left(\frac{X_0}{D \sin i - Y_0 \cos i}\right). \end{aligned} \tag{65}$$

The initial 4-momentum of the photon is $k_0^\mu = \frac{\partial x^\mu}{\partial X^\mu} K_0^\mu$, where $\{x^\mu\} = (t, x, y, z)$, $\{X^\mu\} = (t, X, Y, Z)$ are the Cartesian coordinates of the distant observer, and $K_0^\mu = (K_0, 0, 0, -K_0)$ is the initial 4-momentum of the photon in the reference frame of the distant observer. The result is

$$\begin{aligned} k_0^r &= -\frac{D}{r_0} K_0\,, \\ k_0^\theta &= \frac{1}{\sqrt{X_0^2 + (D \sin i - Y_0 \cos i)^2}} \left[\cos i - (Y_0 \sin i + D \cos i)\frac{D}{r_0^2}\right] K_0\,, \\ k_0^\phi &= \frac{X_0 \sin i}{X_0^2 + (D \sin i - Y_0 \cos i)^2} K_0\,. \end{aligned} \tag{66}$$

k_0^t can be easily obtained from the condition $g_{\mu\nu} k_0^\mu k_0^\nu = 0$ with the metric tensor of flat spacetime

$$k_0^t = \sqrt{\left(k_0^r\right)^2 + r_0^2 \left(k_0^\theta\right)^2 + r_0^2 \sin^2\theta_0 \left(k_0^\phi\right)^2}\,. \tag{67}$$

With the initial conditions in Equations (65)–(67), we can integrate the geodesic equations in the spherical-like coordinates (t, r, θ, ϕ) backwards in time from a point in the image plane of the distant observer to its emission point on the accretion disk. In the Kerr metric in Boyer–Lindquist coordinates, the equations of motion are separable, and we can restrict the attention to the motion in the $r\theta$-plane; the corresponding equations can be solved in terms of elliptic integrals [19]. In general, this is not the case. We can still exploit the fact that the spacetime is stationary and axisymmetric, so we have Equations (15) and (16), which can be rewritten as

$$\frac{dt}{d\lambda'} = \frac{g_{\phi\phi} + b\, g_{t\phi}}{g_{t\phi}^2 - g_{tt} g_{\phi\phi}}\,, \tag{68}$$

$$\frac{d\phi}{d\lambda'} = -\frac{g_{t\phi} + b\, g_{tt}}{g_{t\phi}^2 - g_{tt} g_{\phi\phi}}\,, \tag{69}$$

where $b = L_z/E = -k_\phi/k_t$ is a constant along the photon trajectory, and $\lambda' = E\lambda$ is the normalized affine parameter. For the r and θ coordinates, we have to solve the second-order geodesic equations, which reduces to the following equations for the metric in Equation (1):

$$\frac{d^2r}{d\lambda'^2} = -\Gamma^r_{tt}\left(\frac{dt}{d\lambda'}\right)^2 - \Gamma^r_{rr}\left(\frac{dr}{d\lambda'}\right)^2 - \Gamma^r_{\theta\theta}\left(\frac{d\theta}{d\lambda'}\right)^2 - \Gamma^r_{\phi\phi}\left(\frac{d\phi}{d\lambda'}\right)^2 - 2\Gamma^r_{t\phi}\left(\frac{dt}{d\lambda'}\right)\left(\frac{d\phi}{d\lambda'}\right) - 2\Gamma^r_{r\theta}\left(\frac{dr}{d\lambda'}\right)\left(\frac{d\theta}{d\lambda'}\right), \tag{70}$$

$$\frac{d^2\theta}{d\lambda'^2} = -\Gamma^\theta_{tt}\left(\frac{dt}{d\lambda'}\right)^2 - \Gamma^\theta_{rr}\left(\frac{dr}{d\lambda'}\right)^2 - \Gamma^\theta_{\theta\theta}\left(\frac{d\theta}{d\lambda'}\right)^2 - \Gamma^\theta_{\phi\phi}\left(\frac{d\phi}{d\lambda'}\right)^2 - 2\Gamma^\theta_{t\phi}\left(\frac{dt}{d\lambda'}\right)\left(\frac{d\phi}{d\lambda'}\right) - 2\Gamma^\theta_{r\theta}\left(\frac{dr}{d\lambda'}\right)\left(\frac{d\theta}{d\lambda'}\right), \tag{71}$$

where $\Gamma^\mu_{\nu\rho}$ are the Christoffel symbols of the metric.

6.2. Redshift Factor and Emission Angle

When the photon hits the accreting material on the equatorial plane, we have to calculate the redshift factor g and the emission angle ϑ_e.

If the photon hits the accreting material in the disk region ($r_\mathrm{e} > r_\mathrm{ISCO}$), the redshift factor is

$$g = \frac{E_\mathrm{o}}{E_\mathrm{e}} = \frac{-u^\mu_\mathrm{o} k_\mu}{-u^\mu_\mathrm{e} k_\mu}, \tag{72}$$

where $u^\mu_\mathrm{o} = (1,0,0,0)$ is the 4-velocity of the distant observer, $u^\mu_\mathrm{e} = u^t_\mathrm{e}(1,0,0,\Omega_\mathrm{K})$ is the 4-velocity of the Keplerian material in the accretion disk, and $k_\mu = (k_t, k_r, k_\theta, k_\phi)$ is the conjugate 4-momentum of the photon. k_μ should be evaluated at the detection point in the numerator and at the emission point in the denominator, but actually k_t and k_ϕ are constants of motion, and k_r and k_θ do not play any role as the r and θ components of the 4-velocities of the observer and of the material in the disk vanish. With u^t_e from Equation (20), the redshift factor g is

$$g = \frac{\sqrt{-g_{tt} - 2g_{t\phi}\Omega_\mathrm{K} - g_{\phi\phi}\Omega^2_\mathrm{K}}}{1 - b\,\Omega_\mathrm{K}} \tag{73}$$

where $b = -k_\phi/k_t$ is a constant of motion and can be evaluated, for example, from the initial conditions, so from the last expression in Equation (66) and from Equation (67).

To evaluate the emission angle in the rest-frame of the material in the disk, we need the normal to the disk surface in the rest-frame of the material in the disk, n^μ. We have to consider the locally Minkowskian reference frame associated to the material in the disk (see Appendix A) and $n^\mu = E^\mu_{(\mathrm{Z})}$, so

$$n^\mu = \frac{1}{\sqrt{g_{\theta\theta}}}\begin{pmatrix} 0 \\ 0 \\ 1 \\ 0 \end{pmatrix}. \tag{74}$$

The emission angle ϑ_e can be evaluated as

$$\cos\vartheta_\mathrm{e} = \frac{n^\mu k_\mu}{u^\nu_\mathrm{e} k_\nu} = \frac{g}{\sqrt{g_{\theta\theta}}}\frac{k_\theta}{k_t} = \frac{1}{\sqrt{g_{\theta\theta}}}\frac{\sqrt{-g_{tt} - 2g_{t\phi}\Omega_\mathrm{K} - g_{\phi\phi}\Omega^2_\mathrm{K}}}{1 - b\,\Omega_\mathrm{K}}\frac{k_\theta}{k_t}, \tag{75}$$

where k_θ is the θ component of the conjugate 4-momentum of the photon at the emission point in the disk.

If the photon hits the accreting material in the plunging region ($r_{\rm e} < r_{\rm ISCO}$), the redshift factor is still given by Equation (72), but now the 4-velocity $u^\mu_{\rm e}$ has three non-vanishing components $(u^t_{\rm e}, u^r_{\rm e}, u^\phi_{\rm e})$. The redshift factor is

$$g = \left(u^t_{\rm e} + u^r_{\rm e} \frac{k_r}{k_t} + u^\phi_{\rm e} \frac{k_\phi}{k_t} \right)^{-1}, \tag{76}$$

where $u^t_{\rm e}$, $u^r_{\rm e}$, and $u^\phi_{\rm e}$ are given, respectively, by the expressions in Equations (26) and (27) if the material is in free fall. The locally Minkowskian reference frame associated to the material in the plunging region is different from that reported in Appendix A because $u^r_{\rm e}$ is non-vanishing in the plunging region, and $E^\mu_{(T)} = u^\mu$. However, since $u^\theta_{\rm e}$ is still vanishing, we still have

$$n^\mu = \frac{1}{\sqrt{g_{\theta\theta}}} \begin{pmatrix} 0 \\ 0 \\ 1 \\ 0 \end{pmatrix}, \tag{77}$$

and the emission angle is

$$\cos\vartheta_{\rm e} = \frac{g}{\sqrt{g_{\theta\theta}}} \frac{k_\theta}{k_t} = \frac{1}{\sqrt{g_{\theta\theta}}} \left(u^t_{\rm e} + u^r_{\rm e} \frac{k_r}{k_t} + u^\phi_{\rm e} \frac{k_\phi}{k_t} \right)^{-1} \frac{k_\theta}{k_t}. \tag{78}$$

The first calculations of iron line emissions from plunging regions were reported in Ref. [46]. However, current reflection models normally ignore the radiation from the plunging region because the material is thought to be highly ionized. Indeed, in the plunging region, the material is expected to have a non-negligible radial velocity (see Section 2.4), which can lead to a low rest-mass density (which will be estimated in Section 7.3). In such a case, the ionization parameter ξ must be very high; see Equation (51). If the material is highly ionized, the interactions between the photons from the corona and the material in the plunging region are dominated by Compton scattering: the resulting reflection spectrum has no emission lines and has instead the same shape as the incident spectrum. In the analysis of the X-ray spectrum of a source, the reflection spectrum from the plunging region contributes to the continuum and cannot be easily distinguished from the direct spectrum from the corona. At the same time, it does not affect the analysis of the reflection features from the disk and, in turn, the estimate of the parameters of the model. Such a conclusion may change in the presence of non-negligible magnetic fields in the plunging region, as these magnetic fields may reduce the radial velocity of the accreting material, and thus increase the value of the electron density and decrease the value of the ionization parameter. If magnetic fields can significantly slow down the plunging process, even the reflection spectrum from the plunging region may have emission lines, which may affect the estimate of the parameters of the system if the reflection spectrum from the plunging region is not properly taken into account.

6.3. Examples of Relativistic Reflection Spectra

Figure 9 shows some relativistic reflection spectra produced by the `relxill` model [47] for different values of the black hole spin parameter. The model ignores the radiation from the plunging region and the effect of the returning radiation. These relativistic spectra are calculated from the non-relativistic spectra produced by `xillver`.

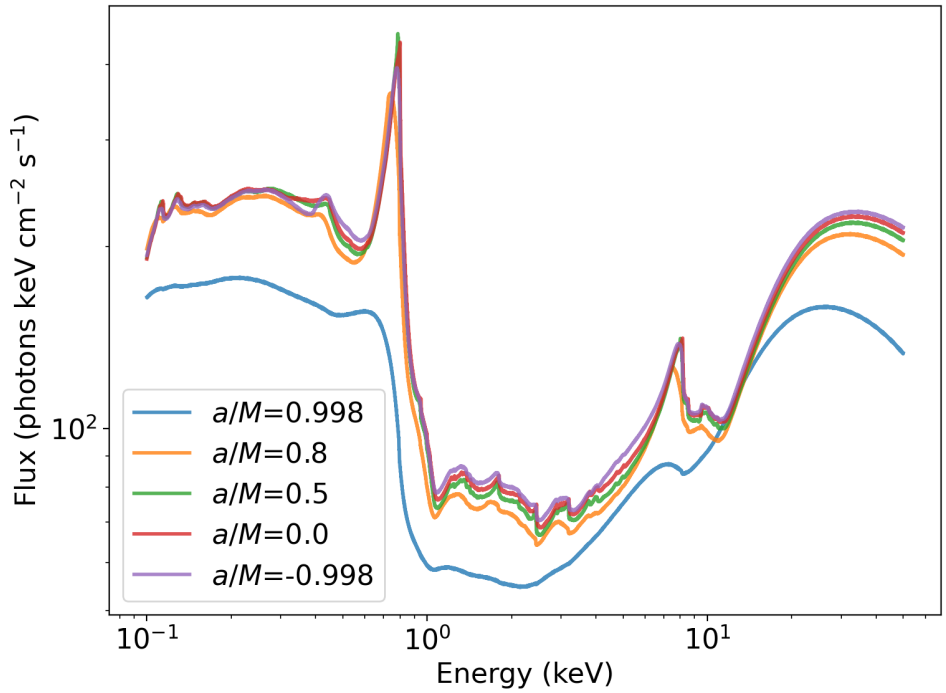

Figure 9. Examples of relativistic reflection spectra produced with `relxill` [47] for different values of the black hole spin parameter $a_* = a/M$ assuming that the disk inclination angle is $i = 60°$, the photon index is $\Gamma = 1.7$, the high-energy cutoff is $E_{\rm cut} = 300$ keV, the emissivity index is $q = 6$ (the emissivity profile is described by a power law, $I_{\rm e} \propto r^{-q}$), the ionization parameter is $\log \xi = 3$ (ξ in units erg cm s^{-1}), and the electron density $\log N = 18$ (N in units of cm^{-3}).

The effect of the returning radiation can be important when the inner edge of the accretion disk is very close to the black hole (which is normally possible only for very fast-rotating black holes) and when the corona illuminates mainly the inner part of the accretion disk (for instance, in the case of a lamppost corona, this is possible when the height of the corona is very low). Reflection spectra can be produced even in the absence of a corona by the returning radiation of the thermal spectrum of the disk. The model `ziji` can calculate reflection spectra from thin disks, taking the returning radiation into account [43,44].

7. Novikov–Thorne Disk

To calculate relativistic reflection spectra, the disk model discussed in Section 2 is enough. We just assume that the disk is infinitesimally thin and perpendicular to the black hole spin axis, and that the material in the disk moves on geodesic equatorial circular orbits. There are no other assumptions. To calculate the relativistic thermal spectra, these ingredients are not enough. We need a disk model predicting the temperature of the disk at any radial coordinate. The Novikov–Thorne disk model addresses this point [1,48]. In this section, we consider a simplified version of the Novikov–Thorne model, and we follow a more heuristic approach than the original publications, without paying attention to all assumptions.We consider an ideal case, in which the system is in a steady-state configuration, while the actual model is valid even if the system is highly dynamical and derives the time-averaged properties of the disk. The details of the complete model can be found in Refs. [1,48].

7.1. Near Equatorial Metric

The line element of our spacetime is given in Equation (1) in spherical-like coordinates (t, r, θ, ϕ). For the discussion of the Novikov–Thorne model, it is convenient to change

the coordinate system and choose cylindrical-like coordinates (t, ρ, z, ϕ). The coordinate transformation is

$$\rho = r \sin\theta\,, \quad z = r\cos\theta\,, \tag{79}$$

with inverse

$$r = \sqrt{\rho^2 + z^2}\,, \quad \theta = \arctan\left(\frac{\rho}{z}\right). \tag{80}$$

Since we are interested in the region near the equatorial plane, we expand the metric coefficients $g_{\rho\rho}$, g_{zz}, and $g_{\rho z}$ around $z = 0$

$$\begin{aligned} g_{\rho\rho} &= \left[1 - \frac{z^2}{\rho^2} + O\left(z^4\right)\right] g_{rr} + \left[\frac{z^2}{\rho^4} + O\left(z^4\right)\right] g_{\theta\theta} = g_{rr} + O\left(z^2\right), \\ g_{zz} &= \left[\frac{z^2}{\rho^2} + O\left(z^4\right)\right] g_{rr} + \left[\frac{1}{\rho^2} - \frac{2z^2}{\rho^4} + O\left(z^4\right)\right] g_{\theta\theta} = \frac{g_{\theta\theta}}{\rho^2} + O\left(z^2\right), \\ g_{\rho z} &= \left[\frac{z}{\rho} + O\left(z^3\right)\right] g_{rr} + \left[-\frac{z}{\rho^3} + O\left(z^3\right)\right] g_{\theta\theta} = O(z)\,. \end{aligned} \tag{81}$$

If we ignore corrections of order z/ρ, the new line element is

$$ds^2 = g_{tt}dt^2 + 2g_{t\phi}dtd\phi + g_{rr}d\rho^2 + \frac{g_{\theta\theta}}{\rho^2}dz^2 + g_{\phi\phi}d\phi^2\,. \tag{82}$$

In many black hole spacetimes (including the Kerr case), $g_{\theta\theta}/\rho^2 = 1$ on the equatorial plane. If this is not the case, we can always introduce the coordinate $dz' = \sqrt{g_{\theta\theta}/\rho^2}\,dz$ to have $g_{z'z'} = 1$. In the end, the line element in cylindrical-like coordinates (t, r, z, ϕ) of our spacetime near the equatorial plane can always be written as

$$ds^2 = \tilde{g}_{tt}dt^2 + 2\tilde{g}_{t\phi}dtd\phi + \tilde{g}_{rr}dr^2 + dz^2 + \tilde{g}_{\phi\phi}d\phi^2\,. \tag{83}$$

where the tilde ˜ is used to indicate the near equatorial metric coefficients in cylindrical-like coordinates (t, r, z, ϕ) and avoid confusion with the metric coefficients in spherical-like coordinates (t, r, θ, ϕ) in Equation (1). The infinitesimal element of the 4-volume of the metric in Equation (83) is

$$dV = \sqrt{-\tilde{g}}\,dt\,dr\,dz\,d\phi = \sqrt{\tilde{g}_{rr}\left(\tilde{g}_{t\phi}^2 - \tilde{g}_{tt}\tilde{g}_{\phi\phi}\right)}\,dt\,dr\,dz\,d\phi\,. \tag{84}$$

7.2. Radial Structure of the Disk

From the laws of conservation of rest-mass $\nabla_\mu(\rho u^\mu) = 0$ conservation of energy $\nabla_\mu T^{t\mu} = 0$, and conservation of angular momentum $\nabla_\mu T^{\phi\mu} = 0$, we can derive the radial structure of the accretion disk [1].

Let us consider the conservation of rest-mass $\nabla_\mu(\rho u^\mu) = 0$, where ρ is the mass density measured in the rest-frame of the material ($\rho = mn$, where m is the mean rest-mass per particle, and n is the particle density in the rest-frame of the material). We integrate this expression over the 4-volume of the spacetime from t_* to $t_* + \Delta t$ and from r_* to $r_* + \Delta r$ shown in Figure 10, where we collapse the z direction

$$0 = \int_V \nabla_\mu(\rho u^\mu)\,\sqrt{-\tilde{g}}\,dt\,dr\,dz\,d\phi = \int_V \frac{\partial}{\partial x^\mu}\left(\sqrt{-\tilde{g}}\rho u^\mu\right) dt\,dr\,dz\,d\phi = \int_\Sigma \sqrt{-\tilde{g}}\rho u^\mu\,d\sigma_\mu\,, \tag{85}$$

where first we use the formula for the covariant divergence of a generic vector A^μ in a generic spacetime with metric $g_{\mu\nu}$ and metric determinant g (see, for instance, Section 5.3 in Ref. [41] for its derivation)

$$\nabla_\mu A^\mu = \frac{1}{\sqrt{-g}} \frac{\partial}{\partial x^\mu} \left(\sqrt{-g} A^\mu \right) , \tag{86}$$

and then we apply Gauss's theorem to convert the integral over the volume V to the integral over its surface Σ. As shown in Figure 10, in our case, we can consider four surfaces: two cylindrical-like surfaces at, respectively, $r = r_*$ and $r = r_* + \Delta r$, and two annulus-like surfaces at, respectively, $t = t_*$ and $t = t_* + \Delta t$. We have, thus, four integrals

$$\begin{aligned} 0 \;=\; & \left[\int_{t_*}^{t_*+\Delta t} dt \int_{-h/2}^{h/2} dz \int_0^{2\pi} d\phi \, \sqrt{-\tilde{g}} \rho u^r \right]_{r=r_*+\Delta r} \\ & - \left[\int_{t_*}^{t_*+\Delta t} dt \int_{-h/2}^{h/2} dz \int_0^{2\pi} d\phi \, \sqrt{-\tilde{g}} \rho u^r \right]_{r=r_*} \\ & + \left[\int_{r_*}^{r_*+\Delta r} dr \int_{-h/2}^{h/2} dz \int_0^{2\pi} d\phi \, \sqrt{-\tilde{g}} \rho u^t \right]_{t=t_*+\Delta t} \\ & - \left[\int_{r_*}^{r_*+\Delta r} dr \int_{-h/2}^{h/2} dz \int_0^{2\pi} d\phi \, \sqrt{-\tilde{g}} \rho u^t \right]_{t=t_*} . \end{aligned} \tag{87}$$

where h is the thickness of our disk and, for simplicity, we can assume that the rest-mass density is $\rho =$ constant for $-h/2 < z < h/2$, and 0 otherwise. In our simple model in the steady state, the last two integrals exactly cancel each other because the integrand is independent of time. The rest-mass accretion rate is

$$\dot{M} = \int_{-h/2}^{h/2} dz \int_0^{2\pi} d\phi \, \sqrt{-\tilde{g}} \rho u^r = 2\pi \sqrt{-\tilde{g}} \rho h u^r , \tag{88}$$

and therefore Equation (87) becomes

$$\Delta t \, \dot{M}(r_* + \Delta r) - \Delta t \, \dot{M}(r_*) = 0 , \tag{89}$$

so the rest-mass accretion rate (88) is independent of r. This could have been expected because there are no disk winds or outflows in our model.

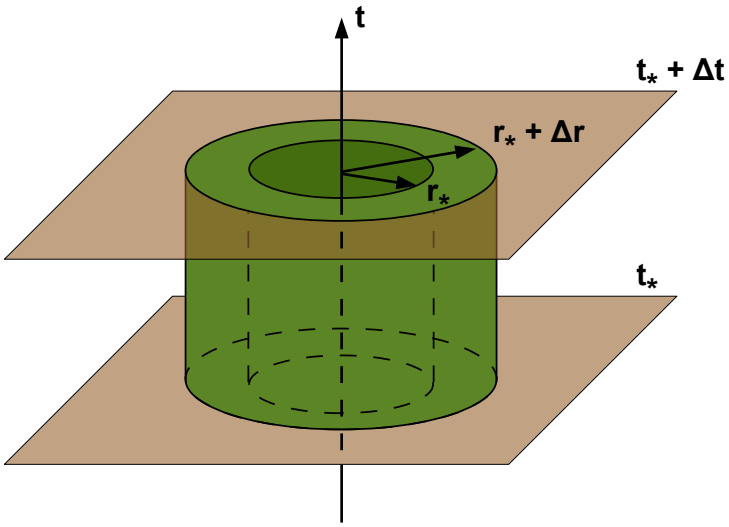

Figure 10. The 4-volume V in Equation (85) is the cylinder-like region of the accretion disk between the surfaces $r = r_*$ and $r = r_* + \Delta r$, and the surfaces $t = t_*$ and $t = t_* + \Delta t$. Figure from Ref. [16].

One can proceed in a similar way with the conservation of energy and angular momentum to find the energy flux from the surface of the accretion disk and the torque at every radial coordinate r. The details can be found in Ref. [1]. To calculate the relativistic thermal spectrum of a disk, we need to have the energy flux from the surface of the disk, which is given by the following expression:

$$\mathcal{F}(r) = \frac{\dot{M}}{4\pi M^2}\,\hat{F}(r)\,, \tag{90}$$

where $\hat{F}$ is the following dimensionless function

$$\hat{F}(r) = -\frac{1}{(E-\Omega_{\rm K}L_z)^2}\frac{\partial\Omega_{\rm K}}{\partial r}\frac{M^2}{\sqrt{-\tilde{g}}}\int_{r_{\rm in}}^{r}(E-\Omega_{\rm K}L_z)\,\frac{\partial L_z}{\partial\varrho}\,d\varrho\,. \tag{91}$$

In Equation (91), E and L_z are, respectively, the specific energy and the axial component of the specific angular momentum for geodesic equatorial circular orbits given in Equations (21) and (22), $\Omega_{\rm K}$ is the Keplerian angular velocity of the material in the disk given in Equation (19), and $r_{\rm in}$ is the inner edge of the accretion disk ($r_{\rm in} \geq r_{\rm ISCO}$).

7.3. Plunging Region

From Equation (88), we can estimate the rest-mass density in the plunging region. If we assume that the radial component of the 4-velocity of the accreting material is given by Equation (28) in the plunging region and h is roughly constant (say $h \sim 0.1$ or $0.01\ M$), the rest-mass density is

$$\rho(r) = \frac{\dot{M}}{2\pi h}\left[\tilde{g}_{\phi\phi}(E^{\rm ISCO})^2 + 2\tilde{g}_{t\phi}E^{\rm ISCO}L_z^{\rm ISCO} + \tilde{g}_{tt}(L_z^{\rm ISCO})^2 - \tilde{g}_{t\phi}^2 + \tilde{g}_{tt}\tilde{g}_{\phi\phi}\right]^{-1/2}. \tag{92}$$

For a fixed background metric, ρ in Equation (92) is only a function of r and $\dot{M}$.

8. Relativistic Thermal Spectrum

If we assume that (i) the material in the accretion disk is in local thermal equilibrium, (ii) the heat transport along the radial direction is negligible, and the energy and angular momentum are radiated from the disk surface, we can define an effective temperature $T_{\rm eff}$ at every radial coordinate by imposing that the energy flux $\mathcal{F}$ in Equation (90) is the heat power emitted from the surface of the disk and using the Stefan–Boltzmann law

$$\mathcal{F} = \sigma_{\rm SB}\,T_{\rm eff}^4\,, \tag{93}$$

where $\sigma_{\rm SB} = 5.67\cdot10^{-5}$ erg s^{-1} cm^{-2} K^{-4} is the Stefan–Boltzmann constant. Figure 11 shows the radial profile of the effective temperature of a Novikov–Thorne disk around a Kerr black hole with mass $M = 10\ M_\odot$ and different values of the black hole spin parameters a_*, assuming that the black hole mass accretion rate is $\dot{M} = 10^{18}$ g s^{-1} and that $r_{\rm in} = r_{\rm ISCO}$. Since Novikov–Thorne disks are realized when the black hole mass accretion rate is of the order of 10% of the Eddington limit of the source, $\mathcal{F}$ turns out to be always proportional to $1/M$, and we can easily see that the effective temperature of the inner part of a Novikov–Thorne disk should be of the order of 1 keV for $M = 10\ M_\odot$ and of the order of 10 eV for $M = 10^9\ M_\odot$

$$T_{\rm eff} \sim 1\left(\frac{10\,M_\odot}{M}\right)^{1/4}{\rm keV}\,. \tag{94}$$

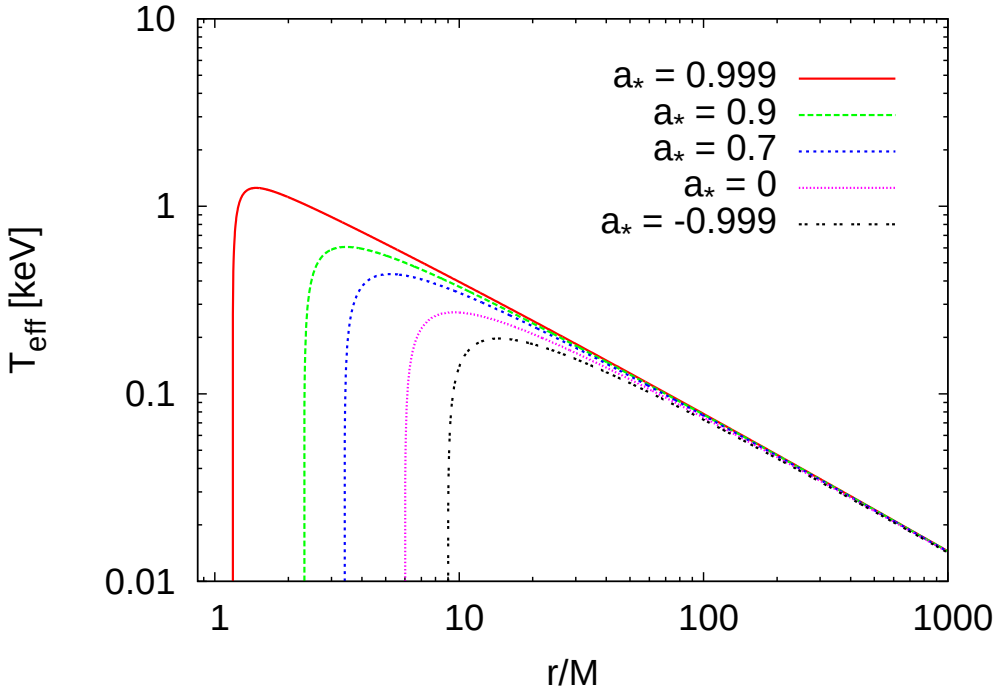

Figure 11. Radial profile of the effective temperature $T_{\rm eff}$ in Novikov–Thorne disks around Kerr black holes with $M = 10\ M_\odot$, $\dot{M} = 10^{18}$ g s^{-1}, and different values of the black hole spin parameters a_*. Figure from Ref. [16].

In the case of accretion disks around stellar-mass black holes, the effective temperature of the inner part is high, and non-thermal effects (mainly electron scattering in the disk atmosphere) cannot be ignored. Deviations from the blackbody spectrum can be taken into account by introducing the *color factor* (or hardening factor) $f_{\rm col}$ and defining the *color temperature* $T_{\rm col} = f_{\rm col} T_{\rm eff}$. The specific intensity of the radiation in the rest-frame of the material in the disk is (for this formula, it can be useful to reintroduce fundamental constants rather than using natural units):

$$I_{\rm e} = \frac{2h\nu_{\rm e}^3}{c^2} \frac{1}{f_{\rm col}^4} \frac{\rm Y}{\exp\left(\frac{h\nu_{\rm e}}{k_{\rm B} T_{\rm col}}\right) - 1}, \tag{95}$$

where h is the Planck constant, c is the speed of light, $k_{\rm B}$ is the Boltzmann constant, and ${\rm Y} = {\rm Y}(\vartheta_{\rm e})$ is a function regulating the angular emission. The two most popular choices are ${\rm Y} = 1$ (isotropic emission) and ${\rm Y} = 0.5 + 0.75 \cos\vartheta_{\rm e}$ (limb-darkened emission). In the case of a 10 $M_\odot$ black hole with an accretion luminosity of 10% its Eddington limit, $f_{\rm col}$ is expected to be in the range 1.5 to 1.9, and it can be evaluated by a model for the disk atmosphere [49–51][13]. Note that $I_{\rm e} = I_{\rm e}(r_{\rm e})$ because $T_{\rm col}$ (and at some level, even $f_{\rm col}$) depends on the radial coordinate.

With $I_{\rm e}$ in Equation (95), we can proceed as in the case of the calculation of a relativistic reflection spectrum discussed in Section 6 and infer the relativistic thermal spectrum of a source through Equation (62). We consider a distant observer and we fire photons from the plane of the distant observer to the accretion disk with the photon initial conditions presented in Section 6.1. When a photon hits the accretion disk ($r > r_{\rm ISCO}$), we calculate the redshift factor g and, if we do not assume ${\rm Y} = 1$, the emission angle $\vartheta_{\rm e}$. We repeat the calculations for every small element $dXdY$ in the image plane of the distant observer, and then we integrate over the full image to obtain the relativistic thermal spectrum of the whole disk. In the Novikov–Thorne model, there is no emission of radiation from the plunging region. However, there is material even there, and one can include the thermal spectrum of the plunging region; see, for instance, the model in Ref. [53].

9. Cunningham's Transfer Function

The calculations of relativistic reflection spectra and of the relativistic thermal spectra of thin disks discussed in the previous sections turn out to be very time-consuming. The geodesic equations are relatively easy and fast to solve, but normally one has to calculate the trajectories of millions of photons to reach the required accuracy in the final result. The calculation of non-relativistic reflection spectra requires solving radiative transfer equations, which are definitively time-consuming. On the other hand, during the data analysis process, we have to be able to quickly generate many spectra for different values of the model parameters in order to scan the full parameter space and find the best-fit model, so we cannot perform the calculations described in the previous sections.

Every point in the image of the accretion disk in the plane of the distant observer is specified by the Cartesian coordinates (X, Y). After calculating the photon trajectories, for every point in the image of the accretion disk, we can associate a point on the accretion disk, and we can determine its emission radius $r_{\rm e}$ and its redshift factor g. In the case of an infinitesimally thin Keplerian accretion disk perpendicular to the spin axis of a Kerr black hole, every point on the accretion disk is visible to a distant observer: the circle of the points with the same emission radius $r_{\rm e}$ will not be a circle in the image of the accretion disk in the plane of the distant observer, but it will still be a closed loop. Moreover, for each of these closed loops, we will have a point with the minimum value of the redshift factor and a point with the maximum value of the redshift factor. Which points on the accretion disk have the minimum and maximum redshift factors depends on the emission radius $r_{\rm e}$ and the inclination angle of the disk i (if we fix the background metric by specifying the black hole spin parameter a_*) because the redshift factor is the result of the competition/combination between the Doppler boosting (which depends on both the emission radius and the inclination angle of the disk) and the gravitational redshift (which depends only on the emission radius). We can thus write $g_{\rm min} = g_{\rm min}(r_{\rm e}, i)$ and $g_{\rm max} = g_{\rm max}(r_{\rm e}, i)$ to indicate the minimum and maximum redshift factor for the emission radius $r_{\rm e}$ and the disk inclination angle i. Since the points on the accretion disk at the same emission radius form a closed loop on the image of the disk in the plane of the observer, the point with the minimum redshift factor and the point with the maximum redshift factor are connected by two branches. It turns out that, in both branches, the redshift factor monotonically increases when we move from the point with the minimum redshift factor to the point with the maximum redshift factor[14]. These results allow us to define the relative redshift factor g^* as

$$g^* = \frac{g - g_{\rm min}}{g_{\rm max} - g_{\rm min}}\,, \tag{96}$$

and to parametrize the points of the accretion disk with the emission radius $r_{\rm e}$ and the relative redshift factor g^*.

We can thus recast Equation (62) in the following form [55–57]:

$$\begin{aligned} F_{\rm o}(\nu_{\rm o}) \;=\; & \frac{1}{D^2}\int_{r_{\rm in}}^{r_{\rm out}} dr_{\rm e} \int_0^1 dg^* \, \frac{\pi r_{\rm e} g^2}{\sqrt{g^*(1-g^*)}} \, f^{(1)}(g^*, r_{\rm e}, i)\, I_{\rm e}(\nu_{\rm e}, r_{\rm e}, \vartheta_{\rm e}^{(1)}) \\ & + \frac{1}{D^2}\int_{r_{\rm in}}^{r_{\rm out}} dr_{\rm e} \int_0^1 dg^* \, \frac{\pi r_{\rm e} g^2}{\sqrt{g^*(1-g^*)}} \, f^{(2)}(g^*, r_{\rm e}, i)\, I_{\rm e}(\nu_{\rm e}, r_{\rm e}, \vartheta_{\rm e}^{(2)})\,, \end{aligned} \tag{97}$$

where f is *Cunningham's transfer function* [56]

$$f^{(i)}(g^*, r_{\rm e}, i) = \frac{g\sqrt{g^*(1-g^*)}}{\pi r_{\rm e}} \left| \frac{\partial(X,Y)}{\partial(r_{\rm e}, g^*)} \right| \tag{98}$$

and at every emission radius, we have two transfer functions $f^{(1)}$ and $f^{(2)}$ because we have two branches connecting $g_{\rm min}$ to $g_{\rm max}$. $r_{\rm in}$ and $r_{\rm out}$ are, respectively, the inner and the other radii of the accretion disk. $|\partial(X,Y)/\partial(r_{\rm e}, g^*)|$ is the Jacobian between the Cartesian

coordinate of the image plane of the distant observer, (X, Y), and the coordinates used on the accretion disk, $(r_{\rm e}, g^*)$. If the specific intensity at the emission point does not depend on the emission radius, then $I_{\rm e} = I_{\rm e}(\nu_{\rm e}, r_{\rm e})$, and we can rewrite Equation (97) as

$$F_{\rm o}(\nu_{\rm o}) = \frac{1}{D^2} \int_{r_{\rm in}}^{r_{\rm out}} dr_{\rm e} \int_0^1 dg^* \, \frac{\pi r_{\rm e} g^2}{\sqrt{g^*(1-g^*)}} \left[f^{(1)}(g^*, r_{\rm e}, i) + f^{(2)}(g^*, r_{\rm e}, i) \right] I_{\rm e}(\nu_{\rm e}, r_{\rm e}) \,. \quad (99)$$

Figures 12 and 13 show some examples of the transfer functions of an infinitesimally thin Keplerian accretion disk in the Kerr spacetime. In Figure 12, we change the values of the inclination angle of the disk i. In Figure 13, we change the value of the black hole spin parameter $a_* = a/M$ (note that $a/M < 0$ means that the black hole spin is anti-parallel to the angular momentum of the disk). The minimum and maximum redshifts are, respectively, at $g^* = 0$ and 1. These two points are connected by two branches. In Figures 12 and 13, dashed lines are for the transfer functions of the upper branches (say $f^{(1)}$), and solid lines are for the transfer functions of the lower branches (say $f^{(2)}$).

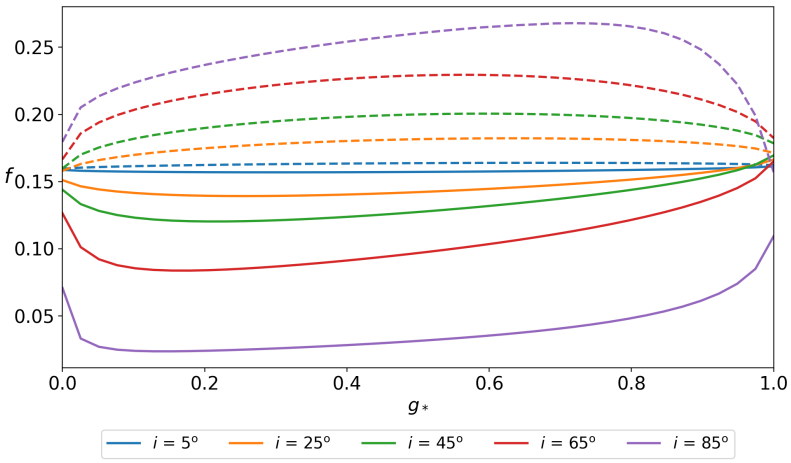

Figure 12. Examples of Cunningham's transfer functions for an infinitesimally thin Keplerian accretion disk in the Kerr spacetime. The central black hole has spin parameter $a_* = 0.998$ and the plot shows the transfer functions at the emission radius $r_{\rm e} = 4\,M$ for different values of the inclination angle of the disk i. Dashed curves are for the upper branches of the transfer functions, and solid curves are for the lower branches.

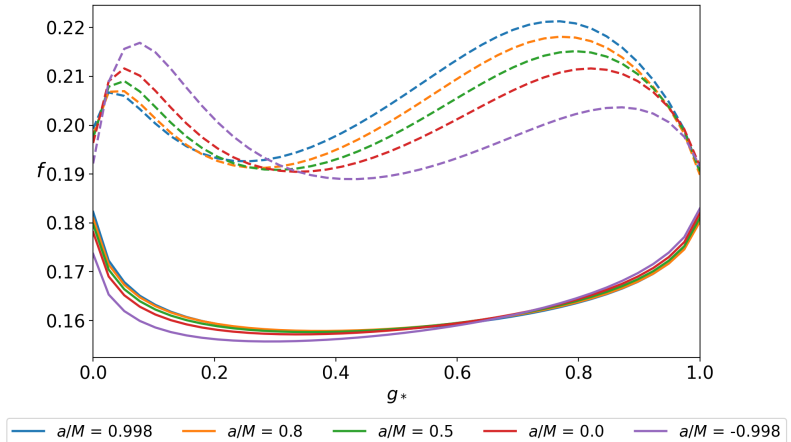

Figure 13. Examples of Cunningham's transfer functions for an infinitesimally thin Keplerian accretion disk in the Kerr spacetime. The inclination angle of the disk is $i = 60^\circ$ and the plot shows the transfer functions at the emission radius $r_{\rm e} = 9\,M$ for different values of the black hole spin parameter $a_* = a/M$. Dashed curves are for the upper branches of the transfer functions, and solid curves are for the lower branches.

In the case of a relativistic thermal model, the specific intensity at the emission point is given by Equation (95). The transfer function f can be pre-calculated and tabulated into a FITS file[15] before the data analysis process. The model for data analysis simply has to solve the integral in Equation (97), or in Equation (99) if $Y = 1$, and call the FITS file to know the value of the transfer function. This is how the model `nkbb` works [58].

For a relativistic reflection model, there are a few complications. The specific intensity at the emission point can be determined after numerically solving radiative transfer equations rather than from a simple analytical formula as in the case of the thermal spectrum. The emissivity profile of the accretion disk can be determined after studying how the corona illuminates the disk. Unlike in the case of the thermal component, we do not know the actual luminosity of the disk in terms of parameters like the black hole mass and the mass accretion rate, and therefore we cannot predict the observed flux as a function of the distance of the source. It is thus convenient to rewrite Equation (97) as

$$\begin{aligned} F_{\rm o}(\nu_{\rm o}) &= C \int_{r_{\rm in}}^{r_{\rm out}} dr_{\rm e} \int_0^1 dg^* \, \frac{\pi r_{\rm e} g^2}{\sqrt{g^*(1-g^*)}} \, f^{(1)}(g^*, r_{\rm e}, i) \, I_{\rm e}(F_{\rm X}, \nu_{\rm e}, r_{\rm e}, \vartheta_{\rm e}^{(1)}) \\ &\quad + C \int_{r_{\rm in}}^{r_{\rm out}} dr_{\rm e} \int_0^1 dg^* \, \frac{\pi r_{\rm e} g^2}{\sqrt{g^*(1-g^*)}} \, f^{(2)}(g^*, r_{\rm e}, i) \, I_{\rm e}(F_{\rm X}, \nu_{\rm e}, r_{\rm e}, \vartheta_{\rm e}^{(2)}) \,, \end{aligned} \tag{100}$$

where C is a normalization constant to be determined when we fit the data, and $F_X = F_X(r_{\rm e})$ is the X-ray spectral flux illuminating the disk at the emission radius $r_{\rm e}$. F_X is determined when we study how the corona and the returning radiation illuminate the disk.

Current reflection models for data analysis often employ a simplification to assume the same non-relativistic reflection spectrum over the whole disk and normalize the specific intensity through the emissivity profile $\epsilon(r_{\rm e})$. Within such an approximation, Equation (100) can be written as

$$F_{\rm o}(\nu_{\rm o}) = C \int_{r_{\rm in}}^{r_{\rm out}} dr_{\rm e} \int_0^1 dg^* \, \frac{\pi r_{\rm e} g^2}{\sqrt{g^*(1-g^*)}} \Big[f^{(1)}(g^*, r_{\rm e}, i) + f^{(2)}(g^*, r_{\rm e}, i) \Big] \epsilon(r_{\rm e}) \, \bar{I}_{\rm e}(\nu_{\rm e}) \,, \tag{101}$$

where $\bar{I}_{\rm e}$ is the "average" specific intensity over the disk (or some region of the disk if we divide the disk into a few zones with different specific intensities). It is evaluated from the weighted sum of specific intensities on the disk (a certain zone of the disk) with different emission angles[16]. Now the transfer function f, the emissivity profile ϵ, and the specific intensity $\bar{I}_{\rm e}$ can be pre-calculated and tabulated into three different FITS files before the data analysis process. In the Kerr spacetime, the transfer function f depends on the black hole spin parameter a_* and the inclination angle of the disk i, and once these two parameters are fixed, it is a function of $r_{\rm e}$ and g^*. The emissivity profile ϵ depends on the parameters of the specific coronal model (for example, in the lamppost setup, it depends only on the height of the corona) and on the background metric (the black hole spin parameters a_* in the case of the Kerr metric): after fixing the coronal model and the background metric, ϵ only depends on the emission radius $r_{\rm e}$. $\bar{I}_{\rm e}$ depends on the X-ray spectral flux illuminating the disk and the parameters of the accretion disk model. For example, if we assume that the X-ray spectral flux illuminating the disk can be approximated by a power law with a high-energy cutoff, we can have five parameters: the photon index Γ, the high-energy cutoff $E_{\rm cut}$, the electron density of the accretion disk N, the ionization parameter ξ, and the iron abundance $A_{\rm Fe}$. During the data analysis process, the model calls the three FITS files in which f, ϵ, and $\bar{I}_{\rm e}$ are tabulated and quickly calculates different relativistic spectra for different values of the model parameters.

The emissivity profile produced by a corona of specific geometry can be calculated with the tools presented in Section 3; see also Refs. [38,59]. If the corona is compact and close to the black hole, the effect of light bending leads to the illumination of mainly the inner part of the accretion disk, and the emissivity profile is very steep [39]. If the corona is compact but not very close to the black hole, at large radii, we recover the Newtonian

limit, where $\epsilon \propto r^{-3}$ [39]. For a corona of unknown geometry, it is common to employ a phenomenological emissivity profile, like a power law ($\epsilon \propto r^{-q}$, where q is the emissivity index), a broken power law ($\epsilon \propto r^{-q_{\rm in}}$ for $r < R_{\rm br}$ and $\epsilon \propto r^{-q_{\rm out}}$ for $r > R_{\rm br}$, where $R_{\rm br}$ is the breaking radius), or a twice broken power law ($\epsilon \propto r^{-q_{\rm in}}$ for $r < R_{\rm br,1}$, $\epsilon \propto r^{-q_{\rm mid}}$ for $R_{\rm br,1} < r < R_{\rm br,2}$, and $\epsilon \propto r^{-q_{\rm out}}$ for $r > R_{\rm br,2}$), where the emissivity index/indices and the breaking radius/radii can be free in the fit and inferred from observations. Steep emissivities ($q > 3$) are commonly found in X-ray binaries [28] and active galactic nuclei [60]. Some observations require extremely steep emissivities in the inner part of the accretion disk (even $q > 10$), which are beyond the values that we could expect from theoretical calculations and may point to some deficiency in our theoretical models.

10. Comparison Between Theoretical Predictions and Observational Data

While this tutorial is focused on the relativistic calculations to predict black hole X-ray spectra, this section is devoted to comparing the predictions of reflection models discussed in the previous sections with real observational data.

In the analysis of real data, we have to model every component of the source, not only the reflection and/or the thermal spectra, and this clearly complicates the analysis of an observation. As an example, here we consider MCG–6–30–15, which is a very bright Seyfert 1 galaxy at redshift $z = 0.007749$. This source has been studied by many authors with different observations and different X-ray missions [24,61–65]. It is the source in which a relativistically broadened iron line was unambiguously detected for the first time [66]. The spectrum of MCG–6–30–15 often shows a very broad and prominent iron Kα line, making this source an excellent candidate to test and study reflection models.

XMM-Newton and *NuSTAR* observed simultaneously MCG–6–30–15 from 29 January 2013 for a total time of ∼315 ks and ∼360 ks, respectively (observation ID 0693781201, 0693781301, and 0693781401 for *XMM-Newton* and 60001047002, 60001047003, and 60001047005 for *NuSTAR*). The first study of these data was reported in Ref. [64]. The quality of the data was very good, but the source was very variable, so the data analysis required some special attention. Here, we report the analysis of Ref. [67]. We arrange the data into four groups according to the flux state of the source (low, medium, high, and very-high flux states) requiring a similar spectral data count for every flux state. The search for the model is described in Ref. [27].

If we fit the data with an absorbed power law, we clearly see a broad iron line peaking around 6 keV and a Compton hump peaking around 20–30 keV; see Figure 14. These are the two typical signatures indicating strong relativistic reflection features in the X-ray spectra of a source. The final model is (in XSPEC language)

$$\texttt{tbabs} \times \texttt{warmabs}_1 \times \texttt{warmabs}_2 \times \texttt{dustyabs} \times \texttt{(cutoffpl+RR+NR+zgauss+zgauss)},$$

where `tbabs` describes the Galactic absorption, $\texttt{warmabs}_1$ and $\texttt{warmabs}_2$ describe two ionized absorbers, `dustyabs` describes a neutral absorber and only modifies the soft X-ray band, `cutoffpl` describes the direct spectrum from the corona, `RR` and `NR` indicate, respectively, a relativistic and a non-relativistic reflection component, and `zgauss` is used to describe a narrow emission line at 0.8 keV and a narrow absorption line at 1.2 keV (for more details, see Ref. [27]). We consider three models. Model 1: we use the `reflionx` model [18] and we have `NR` = `reflionx` and `RR` = `relconv`×`reflionx`. Models 2 and 3: we use `xillver` [17] and `NR` = `xillver`, while `RR` = `relconv`×`xillver` in Model 2 and `RR` = `relxill` in Model 3[17]. For every model, we consider two emissivity profiles: a simple power law ($\epsilon \propto 1/r_{\rm e}^{q}$, where the emissivity index q is a free parameter in the fit) and a broken power law ($\epsilon \propto 1/r_{\rm e}^{q_{\rm in}}$ for $r_{\rm e} < R_{\rm br}$ and $\epsilon \propto 1/r_{\rm e}^{q_{\rm out}}$ for $r_{\rm e} > R_{\rm br}$, where the inner emissivity index $q_{\rm in}$, the outer emissivity index $q_{\rm out}$, and the breaking radius $R_{\rm br}$ are all free parameters in the fit). Figure 15 shows the the best-fitting models of the low flux states and the data to best-fitting model ratios. The six fits provide somewhat similar (even if not completely consistent) estimates of the model parameters (for more details, see Ref. [67]).

The measurements of the spin and of the inclination angle of the disk are reported in Table 1.

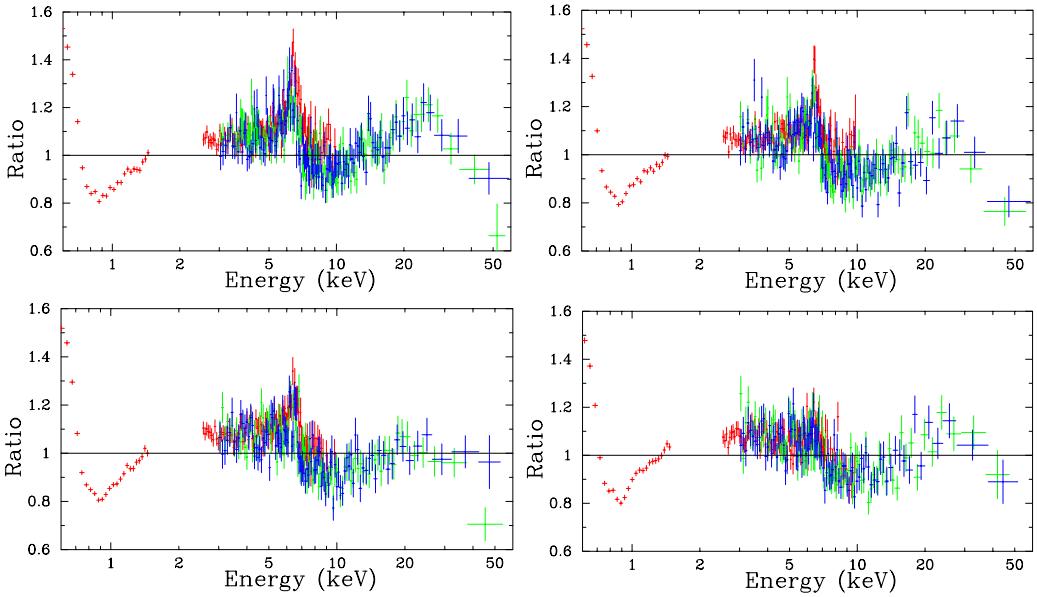

Figure 14. Data to best-fit model ratio for an absorbed power law (in XSPEC language, `tbabs`×`cutoffpl`) for the low flux state (**top left panel**), medium flux state (**top right panel**), high flux state **(bottom left panel**), and very-high flux state (**bottom right panel**). Red crosses are used for *XMM-Newton* data, green crosses are used for *NuSTAR*/FPMA, and blue crosses are used for *NuSTAR*/FPMB. Figure from Ref. [67].

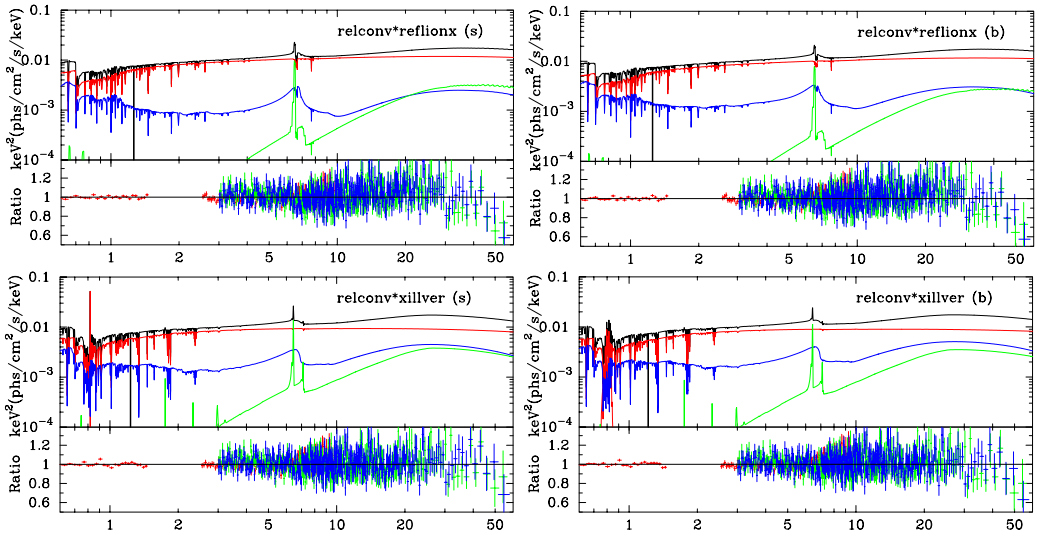

Figure 15. *Cont*.

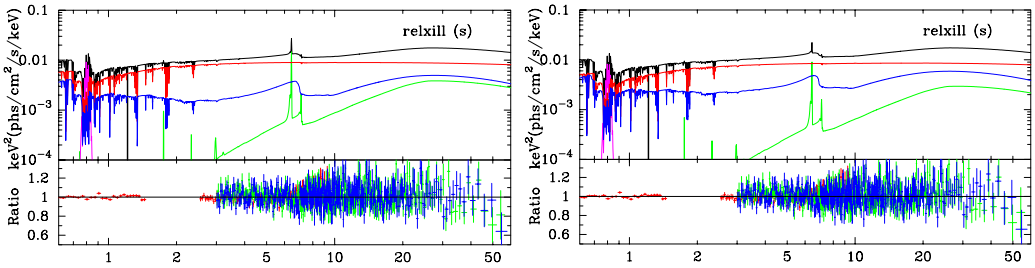

Figure 15. Best-fit models of the low flux state and data to best-fit model ratios for Model 1 (**top panels**), Model 2 (**central panels**), and Model 3 (**bottom panels**), where the emissivity profile is modeled by a simple power law (**left panels**) or a broken power law (**right panels**). In every panel, the total spectrum is in black, the power-law component from the corona is in red, the relativistic reflection component from the disk is in blue, and the non-relativistic reflection component from cold material is in green. Red crosses are used for *XMM-Newton* data, green crosses are used for *NuSTAR*/FPMA, and blue crosses are used for *NuSTAR*/FPMB. Figure from Ref. [67].

Table 1. Best-fit values of the black hole spin parameter a_* and of the inclination angle of the disk i for Model 1 (`NR = reflionx` and `RR = relconv×reflionx`), Model 2 (`NR = xillver` and `RR = relconv×xillver`), and Model 3 (`NR = xillver` and `RR = relxill`). For every model, the emissivity profile can be either a simple power law (s) or a broken power law (b). The reported uncertainties correspond to the 90% confidence level for one relevant parameter ($\Delta\chi^2 = 2.71$). (P) means that the 90% confidence level reaches the maximum value of the parameter in the model. The table also shows the value of χ^2, the number of degree of freedom (dof), and the value of the reduced χ^2. See Ref. [67] for more details.

	Model 1		**Model 2**		**Model 3**	
	s	**b**	**s**	**b**	**s**	**b**
a_*	$0.83^{+0.03}_{-0.04}$	$0.88^{+0.04}_{-0.08}$	$0.90^{+0.06}_{-0.07}$	$0.915^{+0.024}_{-0.030}$	$0.997^{+(P)}_{-0.04}$	$0.962^{+0.019}_{-0.017}$
i [deg]	$24.2^{+1.6}_{-1.7}$	19^{+5}_{-5}	$29.0^{+2.2}_{-2.3}$	$30.7^{+2.2}_{-2.5}$	$33.3^{+1.6}_{-1.6}$	$28.7^{+1.7}_{-1.0}$
χ^2	3171.36	3130.26	3094.68	3079.54	3081.74	3024.46
dof	2691	2683	2689	2681	2691	2683
χ^2/dof	1.17850	1.16670	1.15087	1.14865	1.14520	1.12727

10.1. Requirements in the Analysis of Reflection Features with Current Reflection Models

Reflection models have several parameters. If we want to measure all parameters from the spectral fitting, we need high-quality data and a spectrum with strong signatures of relativistic effects. Without these two ingredients, we are unlikely to be able to break the parameter degeneracy of the model, and we would be forced to freeze the values of some parameters in the fit, with the result that the final measurement may be biased.

To have high-quality data, the source must be very bright to have a good statistics (assuming that our X-ray detector has no pile-up problems), the data should cover a wide energy band to see both the relativistically broadened iron line and the Compton hump, and we should have a good energy resolution at the iron line (which is the most informative part of the spectrum concerning relativistic effects).

In order to have strong relativistic signatures in the reflection spectrum, it is necessary that the inner edge of the accretion disk is as close as possible to the black hole (which, in turn, requires selecting very fast-rotating black holes with an inner edge of the disk at the ISCO radius) and that the corona well illuminates the very inner part of the disk (which, in turn, requires that the corona is compact and very close to the black hole, so the strong light bending can focus most of the hard X-ray photons from the corona to the region around the inner edge of the disk). These two conditions lead to very broadened iron lines in reflection spectra [39]. In the presence of strong relativistic signatures in the reflection spectrum, it is possible to break the parameter degeneracy [68,69].

Since our reflection models assume that the disk is thin, we should only analyze sources with geometrically thin accretion disks. This condition can be satisfied if we select sources with an accretion luminosity between ∼5% and ∼30% of the Eddington limit [70], but this requires having a reliable estimate of the black hole mass and distance. The exact thickness of the disk is not relevant in the final measurement as long as the disks are thin, especially if we study very fast-rotating black holes [54,71]. On the contrary, if the black hole accretes from a thick disk, we can easily obtain precise but non-accurate measurements of the source [72,73].

10.2. Accuracy of the Theoretical Models

Reflection models have been significantly developed in the past decade [23], but they still rely on a number of simplifications that may somewhat affect the final measurements. Even in the example of MCG–06–30–15 at the beginning of this section, we see that the choice of the reflection model may give somewhat different estimates of some parameters.

The geometry of the corona is not yet well understood, though it is important in the calculation of reflection spectra because it determines the exact emissivity profile of the disk. However, the emissivity profiles produced by specific coronal geometries have been calculated in a number of studies [13,38,59,74], and the conclusion is that a broken power law (or a twice broken power law) profile should be enough to well approximate the emissivity profile generated by a corona of arbitrary geometry. In the presence of high-quality data, the fit should be able to determine all parameters of this phenomenological emissivity profile. For example, in Ref. [28], it is shown that the spectra that seem to require a lamppost corona can be also fit with a broken power law profile, always finding consistent estimates of the model parameters, even if the fit is a bit worse (however, the opposite is not true, namely, the spectra that require a broken power law profile may not fit with the less flexible lamppost model).

The accuracy of the disk model employed in reflection models was recently tested with *NuSTAR* simulations of reflection spectra calculated from GRMHD-simulated disks in Ref. [37]. The conclusion of that work is that we can recover the correct input parameters from the spectral analysis of the reflection features with the current reflection models. The concept of the inner edge of the disk is more likely replaced by the "reflection edge", which is still around the ISCO radius and separates the disk from the plunging region [75]. The plunging region can be optically thick and produce reflection photons, but its density is so low that the gas is highly ionized: as a result, the reflection process is dominated by Compton scattering, and the reflection spectrum looks like a power law without emission lines, so it does not affect the analysis of the reflection features and, in turn, the estimate of the model parameters [75,76].

The effect of the returning radiation (discussed in Section 5) is normally ignored in the analysis of current black hole X-ray spectra. In the case of thermal spectra, it was shown that a thermal spectrum calculated taking the returning radiation into account is very similar to a thermal spectrum calculated without including the returning radiation and a slightly higher mass accretion rate [77]. The effect is therefore ignored because it does not affect the measurement of black hole spins. In the case of the reflection spectra, the returning radiation has two effects: it alters the original emissivity profile produced by the corona and changes the reflection spectrum itself because the direct spectrum from the corona illuminating the disk can be approximated by a power law with a high-energy cutoff but the spectrum of the returning radiation is a reflection spectrum. Moreover, even the thermal radiation can return to the disk and produce reflection radiation, and we may have a reflection spectrum even without a corona and entirely generated by the returning radiation of the thermal component. Recently, the reflection model `relxill` included the effect of the returning radiation on the emissivity profile of the disk, still assuming that the reflection spectrum is produced by a power law spectrum with a high-energy cutoff [78]. The model `ziji` can calculate reflection spectra, taking the returning radiation of both the reflection and thermal component into account [43,44], but it is too slow to analyze data.

However, it was shown that the analysis of data with a reflection model that ignores the returning radiation or considers only the effect of the returning radiation in the emissivity profile of the disk can significantly overestimate or underestimate some model parameters, especially in the case of fast-rotating black holes with compact coronae close to the inner part of the accretion disk, which are the kind of systems for which we can have more precise measurements [43,44].

11. Concluding Remarks

This tutorial reviews the relativistic calculations of the electromagnetic spectrum of cold, thin, Keplerian accretion disks around black holes. The disk–corona model predicts a thermal spectrum from the disk, a Comptonized spectrum from the hot corona, and a relativistically blurred reflection spectrum from the disk. The expressions reported in this tutorial are valid for a generic stationary, axisymmetric, asymptotically flat, circular black hole spacetime, and therefore they can be potentially applied to a large class of black hole solutions. The presentation is intentionally pedagogical in order to help graduate students to enter this line of research. More details can be found in the papers in the reference list. As pointed out in this tutorial, current models for data analysis present many simplifications in order to be able to quickly produce many spectra. Some improvements are already required for the analysis of *XRISM* data: the microcalorimeter on *XRISM* [79] has an energy resolution of around 5 eV at the iron line, but current non-relativistic reflection models have tables with an energy resolution of up to 20 eV at the iron line. The analysis of data of future X-ray missions like *Athena* [80] will require significantly more advanced models than those available today.

Funding: This work was supported by the Natural Science Foundation of Shanghai, Grant No. 22ZR1403400, and the National Natural Science Foundation of China (NSFC), Grant Nos. 12250610185 and 12261131497.

Data Availability Statement: No new data were used or generated in this article.

Conflicts of Interest: The author declares no conflicts of interest.

Appendix A. Locally Minkowskian Reference Frames

There are situations in which it is convenient to choose the reference frame of a locally Minkowskian observer. Formally, this is equivalent to a coordinate transformation from the coordinate system $\{x^\mu\}$ to the coordinate system $\{x'^\mu\} = (T, X, Y, Z)$[18]

$$dx^\mu \to dx'^{(\alpha)} = E^{(\alpha)}_\mu dx^\mu \,, \tag{A1}$$

such that the new metric tensor is the Minkowski metric

$$g_{\mu\nu} \to \eta_{(\alpha)(\beta)} = E^\mu_{(\alpha)} E^\nu_{(\beta)} g_{\mu\nu} \,, \tag{A2}$$

where $E^\mu_{(\alpha)}$ are the inverse of $E^{(\alpha)}_\mu$, so $E^{(\alpha)}_\mu E^\nu_{(\alpha)} = \delta^\nu_\mu$ and $E^{(\alpha)}_\mu E^\mu_{(\beta)} = \delta^{(\alpha)}_{(\beta)}$. $\{E^\mu_{(\alpha)}\}$ is the *tetrad* of the orthogonal basis vectors associated to the reference frame of the locally Minkowskian observer. If a vector (dual vector) has components V^μ (V_μ) in the coordinate system $\{x^\mu\}$, the components of the vector (dual vector) in the locally Minkowskian reference frame are

$$V^{(\alpha)} = E^{(\alpha)}_\mu V^\mu \,, \quad V_{(\alpha)} = E^\mu_{(\alpha)} V_\mu \,. \tag{A3}$$

It is straightforward to see that

$$V^\mu = E^\mu_{(\alpha)} V^{(\alpha)} \,, \quad V_\mu = E^{(\alpha)}_\mu V_{(\alpha)} \,. \tag{A4}$$

Note that the spacetime indices are lowered by $g_{\mu\nu}$ and raised by $g^{\mu\nu}$, and the internal indices of the locally Minkowskian reference frame are lowered by $\eta_{(\alpha)(\beta)}$ and raised by $\eta^{(\alpha)(\beta)}$.

The time-like tetrad basis vector $E^{\mu}_{(T)}$ is the 4-velocity of the locally Minkowskian observer in the coordinate system $\{x^{\mu}\}$, say, u^{μ}. In our case, the spacetime metric is given in Equation (1) in spherical-like coordinates (t, r, θ, ϕ). If the locally Minkowskian observer is in a circular orbit (not necessarily on the equatorial plane), his/her 4-velocity is $u^{\mu} = u^{t}\,(1, 0, 0, \omega)$, where u^{t} can be inferred from $g_{\mu\nu}\dot{x}^{\mu}\dot{x}^{\nu} = -1$

$$u^{t} = \frac{1}{\sqrt{-g_{tt} - 2g_{t\phi}\omega - g_{\phi\phi}\omega^{2}}} \tag{A5}$$

and $\omega = u^{\phi}/u^{t}$ is the angular velocity of the observer with respect to the coordinate system (t, r, θ, ϕ)[19]. A natural choice for the tetrad of the orthogonal basis vectors associated to the reference frame of the locally Minkowskian observer is

$$E^{\mu}_{(T)} = u^{t}\begin{pmatrix} 1 \\ 0 \\ 0 \\ \omega \end{pmatrix}, \quad E^{\mu}_{(X)} = \frac{1}{\sqrt{g_{rr}}}\begin{pmatrix} 0 \\ 1 \\ 0 \\ 0 \end{pmatrix}, \quad E^{\mu}_{(Y)} = \frac{u^{t}}{\sqrt{g^{2}_{t\phi} - g_{tt}g_{\phi\phi}}}\begin{pmatrix} g_{t\phi} + \omega g_{\phi\phi} \\ 0 \\ 0 \\ -g_{tt} - \omega g_{t\phi} \end{pmatrix},$$
$$E^{\mu}_{(Z)} = \frac{1}{\sqrt{g_{\theta\theta}}}\begin{pmatrix} 0 \\ 0 \\ 1 \\ 0 \end{pmatrix}. \tag{A6}$$

The inverse is

$$E^{(T)}_{\mu} = -u^{t}\begin{pmatrix} g_{tt} + \omega g_{t\phi} \\ 0 \\ 0 \\ g_{t\phi} + \omega g_{\phi\phi} \end{pmatrix}, \quad E^{(X)}_{\mu} = \sqrt{g_{rr}}\begin{pmatrix} 0 \\ 1 \\ 0 \\ 0 \end{pmatrix}, \quad E^{(Y)}_{\mu} = u^{t}\sqrt{g^{2}_{t\phi} - g_{tt}g_{\phi\phi}}\begin{pmatrix} -\omega \\ 0 \\ 0 \\ 1 \end{pmatrix},$$
$$E^{(Z)}_{\mu} = \sqrt{g_{\theta\theta}}\begin{pmatrix} 0 \\ 0 \\ 1 \\ 0 \end{pmatrix}. \tag{A7}$$

A special case is an observer with angular velocity $\omega = \Omega_{\mathrm{LNRF}} = -g_{t\phi}/g_{\phi\phi}$, which is often referred to as a *locally non-rotating frame* (LNRF) in the literature [34][20]. The 4-velocity of such an observer is

$$u^{t} = \sqrt{\frac{g_{\phi\phi}}{g^{2}_{t\phi} - g_{tt}g_{\phi\phi}}}. \tag{A8}$$

The tetrad of the orthogonal basis vectors associated to the locally non-rotating observer reduces to

$$E^{\mu}_{(T)} = \sqrt{\frac{g_{\phi\phi}}{g^{2}_{t\phi} - g_{tt}g_{\phi\phi}}}\begin{pmatrix} 1 \\ 0 \\ 0 \\ \omega \end{pmatrix}, \quad E^{\mu}_{(X)} = \frac{1}{\sqrt{g_{rr}}}\begin{pmatrix} 0 \\ 1 \\ 0 \\ 0 \end{pmatrix}, \quad E^{\mu}_{(Y)} = \frac{1}{\sqrt{g_{\phi\phi}}}\begin{pmatrix} 0 \\ 0 \\ 0 \\ 1 \end{pmatrix},$$
$$E^{\mu}_{(Z)} = \frac{1}{\sqrt{g_{\theta\theta}}}\begin{pmatrix} 0 \\ 0 \\ 1 \\ 0 \end{pmatrix}, \tag{A9}$$

with inverse

$$E^{(T)}_{\mu} = \sqrt{\frac{g^2_{t\phi} - g_{tt}g_{\phi\phi}}{g_{\phi\phi}}} \begin{pmatrix} 1 \\ 0 \\ 0 \\ 0 \end{pmatrix}, \quad E^{(X)}_{\mu} = \sqrt{g_{rr}} \begin{pmatrix} 0 \\ 1 \\ 0 \\ 0 \end{pmatrix}, \quad E^{(Y)}_{\mu} = \sqrt{g_{\phi\phi}} \begin{pmatrix} -\omega \\ 0 \\ 0 \\ 1 \end{pmatrix},$$
$$E^{(Z)}_{\mu} = \sqrt{g_{\theta\theta}} \begin{pmatrix} 0 \\ 0 \\ 1 \\ 0 \end{pmatrix}. \tag{A10}$$

Appendix B. Proper Areas of the Annuli of an Accretion Disk

Let us consider an observer in an equatorial circular orbit with Keplerian angular velocity. The tetrad and the inverse of the tetrad associated to such an observer are given in Equations (A6) and (A7) with $\omega = \Omega_{\rm K}$, where $\Omega_{\rm K}$ is the angular velocity in Equation (19).

First, we want to figure out the proper length of the orbit of this observer. At a certain time $t = t_*$, in the coordinate system (t, r, θ, ϕ), we measure the angle $d\phi$. In his/her locally Minkowskian reference frame, the observer measures

$$dY = E^{(Y)}_{\mu} dx^{\mu} = u^t \sqrt{g^2_{t\phi} - g_{tt}g_{\phi\phi}}\, d\phi = \sqrt{\frac{g^2_{t\phi} - g_{tt}g_{\phi\phi}}{-g_{tt} - 2g_{t\phi}\Omega_{\rm K} - g_{\phi\phi}\Omega^2_{\rm K}}}\, d\phi\,, \tag{A11}$$

because $dt = 0$. If the radial coordinate of the orbit is $r = r_i$, the proper length of the orbit of the observer is

$$\ell(r_i) = \int_0^{2\pi} d\phi \sqrt{\frac{g^2_{t\phi} - g_{tt}g_{\phi\phi}}{-g_{tt} - 2g_{t\phi}\Omega_{\rm K} - g_{\phi\phi}\Omega^2_{\rm K}}} = 2\pi \left[\sqrt{\frac{g^2_{t\phi} - g_{tt}g_{\phi\phi}}{-g_{tt} - 2g_{t\phi}\Omega_{\rm K} - g_{\phi\phi}\Omega^2_{\rm K}}} \right]_{r=r_i, \theta=\pi/2}. \tag{A12}$$

Second, we want to figure out how the same observer measures distances perpendicular to his/her trajectory. If in the coordinate system (t, r, θ, ϕ) we measure dr, the observer measures

$$dX = \sqrt{g_{rr}} dr\,. \tag{A13}$$

We can now combine these two results to evaluate the proper area of an annulus of a Keplerian accretion disk with radial coordinate r_i and width Δr_i:

$$\begin{aligned} A(r_i, \Delta r_i) &= \int_0^{2\pi} d\phi \int_{r_i}^{r_i + \Delta r_i} dr\, \sqrt{g_{rr}} \sqrt{\frac{g^2_{t\phi} - g_{tt}g_{\phi\phi}}{-g_{tt} - 2g_{t\phi}\Omega_{\rm K} - g_{\phi\phi}\Omega^2_{\rm K}}} \\ &= 2\pi\Delta r_i \left[\sqrt{\frac{g_{rr}\left(g^2_{t\phi} - g_{tt}g_{\phi\phi}\right)}{-g_{tt} - 2g_{t\phi}\Omega_{\rm K} - g_{\phi\phi}\Omega^2_{\rm K}}} \right]_{r=r_i, \theta=\pi/2}. \end{aligned} \tag{A14}$$

This result is used in Equation (48).

In the existing literature, the calculation of $A(r_i, \Delta r_i)$ is normally proposed with a slightly different approach. First, we consider a locally non-rotating observer on the equatorial plane. The angular velocity of such an observer is $\omega = \Omega_{\rm LNRF} = -g_{t\phi}/g_{\phi\phi}$ and the tetrad and the inverse of the tetrad are given in Equations (A9) and (A10), respectively. If in the coordinate system (t, r, θ, ϕ) we measure the angle $d\phi$, in his/her locally Minkowskian reference frame, the locally non-rotating observer measures

$$dY^{\rm LNRF} = E^{(Y)}_{\mu} dx^{\mu} = \sqrt{g_{\phi\phi}}\, d\phi\,. \tag{A15}$$

The proper length of the orbit of the locally non-rotating observer with radial coordinate $r = r_i$ is

$$\ell^{\rm LNRF} = \int_0^{2\pi} d\phi \, \sqrt{g_{\phi\phi}} = 2\pi \left[\sqrt{g_{\phi\phi}}\right]_{r=r_i,\theta=\pi/2} \tag{A16}$$

Concerning length measurements perpendicular to his/her trajectory, if in the coordinate system (t, r, θ, ϕ) we measure dr, the locally non-rotating observer measures

$$dX^{\rm LNRF} = \sqrt{g_{rr}}\, dr \,. \tag{A17}$$

If we consider a Keplerian accretion disk, the velocity of the material of the disk with respect to the locally non-rotating observer is $u^{(\alpha)} = E^{(\alpha)}_\mu u^\mu$, where $E^{(\alpha)}_\mu$ is given in Equation (A10), $u^\mu = u^t(1, 0, 0, \Omega_{\rm K})$ is the 4-velocity of the material in the coordinate system (t, r, θ, ϕ), and u^t is given in Equation (20). Since in a Minkowskian (or locally Minkowskian) reference frame, the temporal component of the 4-velocity of a particle corresponds to its Lorentz factor [41], we can evaluate the Lorentz factor γ of the material of the accretion disk measured by the locally non-rotating observer as

$$\gamma = u^{(T)} = E^{(T)}_\mu u^\mu = \left[\sqrt{\frac{g_{t\phi}^2 - g_{tt} g_{\phi\phi}}{g_{\phi\phi}\left(-g_{tt} - 2 g_{t\phi}\Omega_{\rm K} - g_{\phi\phi}\Omega_{\rm K}^2\right)}} \right]_{r=r_i,\theta=\pi/2} . \tag{A18}$$

The proper area of an annulus of a Keplerian accretion disk with radial coordinate r_i and width Δr_i can be evaluated as

$$A(r_i, \Delta r_i) = \gamma A^{\rm LNRF}(r_i, \Delta r_i) \,, \tag{A19}$$

where $A^{\rm LNRF}(r_i, \Delta r_i)$ is the proper area of the annulus with radial coordinate r_i and width Δr_i in the rest-frame of the locally non-rotating observer

$$A^{\rm LNRF}(r_i, \Delta r_i) = \int_0^{2\pi} d\phi \int_{r_i}^{r_i+\Delta r_i} dr \, \sqrt{g_{rr} g_{\phi\phi}} = 2\pi \left[\sqrt{g_{rr} g_{\phi\phi}}\right]_{r=r_i,\theta=\pi/2} \Delta r_i \,. \tag{A20}$$

Equation (A19) is equivalent to Equation (A14), of course.

Notes

1 Generally speaking, an accretion disk is geometrically thin if $h/r \ll 1$, where h is the thickness of the disk at the radial coordinate r, and is optically thick is $h \gg \lambda$, where λ is the photon mean free path in the disk. The accretion disk is instead geometrically thick if $h/r \gtrsim 1$. The accretion disk is optically thin if $h \ll \lambda$.

2 This is normally a very acceptable approximation. Let us consider, for example, a 10 $M_\odot$ black hole in an X-ray binary. Its Eddington luminosity is $L_{\rm Edd} \sim 10^{39}$ erg s^{-1}. Its Eddington mass accretion rate can be found from the relation $L_{\rm Edd} = \eta \dot{M}_{\rm Edd}$, where $\eta \sim 0.1$ is the radiative efficiency, and we have $\dot{M}_{\rm Edd} \sim 10^{-7}\ M_\odot$/yr. In a typical outburst of a black hole binary, the luminosity of the source is around 10% of its Eddington limit and the outburst lasts for about a month, so the total mass in the accretion disk is roughly $10^{-9}\ M_\odot$ and the ratio between the mass of the disk and the mass of the black hole is of order 10^{-10}. Even if the mass of the disk were confined in a relatively small space region (which is not the case), it could produce only a very small perturbation on the background metric. We can thus conclude that the gravitational field of the disk can be ignored. See, for instance, Ref. [32] for more details.

3 We note that we are not considering the motion of the single particles in the accretion disk (ions and electrons) but the motion of a "parcel" of particles.

4 We use the term "specific" because the Lagrangian of a point-like free particle is $\mathcal{L} = \frac{1}{2} m \left(g_{tt}\dot{t}^2 + 2 g_{t\phi}\dot{t}\dot{\phi} + g_{rr}\dot{r}^2 + g_{\theta\theta}\dot{\theta}^2 + g_{\phi\phi}\dot{\phi}^2\right)$, and we set $m = 1$ in Equation (12).

5 Here we ignore the "quasi" and we assume that the material in the disk follows geodesic equatorial circular orbits. However, the "quasi" is important to have accretion onto the black hole. It is indeed necessary a mechanism to transport energy and angular momentum outward, so the material of the disk can slowly inspiral onto the black hole. In reality, the *magnetorotational instability* is the mechanism responsible to transport energy and angular momentum outward and to permit the accretion process [33].

[6] The subindex K is used to indicate that this is the *Keplerian* angular velocity of the material in the accretion disk and to avoid confusion in the formulas between such a quantity and the infinitesimal solid angle $d\Omega$.

[7] If the emission is isotropic, we can divide the sky of every emission point in small solid angles $\Delta\Omega =$ constant and fire a photon from each of these directions. Since $d\Omega = \sin\chi \, d\chi \, d\psi$, we need a grid of constant $\Delta(\cos\chi)$ and $\Delta\psi$.

[8] For the proper area of an annulus in the plunging region, we can consider a locally non-rotating observer as described in Appendix B and evaluate the Lorentz factor γ with Equation (A18) by using the 4-velocity of the material in the plunging region for u^μ.

[9] In models in which gravity does not universally couple to matter, we can have, for example, the phenomenon of variation of "fundamental" constants, namely constants like the fine structure constant α, the electron mass m_e, etc., may not be actual constants and may change in space and/or time [42]. For example, their value in the strong gravitational field of a black hole may be different from their value in our laboratories on Earth. In such a context, the atomic physics may depend on the gravitational field.

[10] The public version of `xillver` has several "flavors". One can choose among three types of incident spectra: (i) a power law with a high-energy cutoff (2 parameters: photon index Γ and high-energy cutoff $E_{\rm cut}$); (ii) a Comptonized spectrum (2 parameters: photon index Γ and electron temperature of the corona $kT_{\rm e}$, while the temperature of the seed photons is $kT_{\rm s} = 10$ eV); a blackbody spectrum (1 parameter: blackbody temperature $kT_{\rm bb}$). The cold material is characterized by the ionization parameter ξ, the iron abundance $A_{\rm Fe}$ (while all other elements have Solar abundances), and in some flavors there is also the electron density N. The emission angle $\vartheta_{\rm e}$ is another parameter of the model, while the incident angle is $\vartheta_{\rm i} = 45^\circ$ and cannot be changed.

[11] While current X-ray observatories do not have the necessary angular resolution to resolve the accretion disk of a black hole and the system appears as a point-like source, we have to consider an ideal observer with an excellent angular resolution in order to calculate the theoretical spectrum of an accretion disk within our model.

[12] Starting from Ref. [45], ray-tracing codes to calculate images of accretion disks around black holes have been significantly developed and today there are a number of public codes that can do these calculations.

[13] In the soft state, when the X-ray spectrum of black hole X-ray binaries is dominated by the thermal spectrum of the disk, powerful disk winds are common [52]. While current calculations of the color factor ignore disk winds, the latter may affect the color temperature.

[14] These results, strictly speaking, are valid in the case of infinitesimally thin Keplerian accretion disk in Kerr spacetimes. They are normally valid even in the case of infinitesimally thin Keplerian accretion disk in non-Kerr spacetimes, but exceptions are possible. In the case of accretion disks of a finite thickness, some parts of the disk may not be visible to a distant observer, so the image of the points on the accretion disk at the same emission radius may not be a closed loop [54].

[15] FITS (Flexible Image Transport System) is a common format for astronomical data files that can store multidimensional arrays and tables.

[16] This approach is motivated by the need to be able to calculate quickly a relativistic reflection spectrum. Note that the ionization parameter is $\xi(r) = 4\pi F/n$, where F is the total flux illuminating the disk at the radial coordinate r and n is the electron density of the disk at the same radial coordinate. A model in which the ionization parameter ξ and the disk electron density n are constant over the disk would require that F is constant too. This is not how most of the current models work: they employ $\bar{I}_{\rm e}$, which is calculated for certain values of ξ and n, and model the emissivity profile with $\epsilon(r_{\rm e})$.

[17] In Model 1, we have the inclination angle of the disk i in `relconv`, while `reflionx` does not have the emission angle $\vartheta_{\rm e}$ as a parameter of the model. In Model 2, the value of the inclination angle of the disk i in `relconv` is tied to that of the emission angle $\vartheta_{\rm e}$ in `xillver`, even if the two angles are different, in general, and $\vartheta_{\rm e}$ should change value over the disk. In Model 3, there is only the inclination angle of the disk i in `relxill`: the model calculates the averaged emission angle and extracts the corresponding spectrum from the `xillver` table.

[18] The transformation (A1) reduces the metric tensor $g_{\mu\nu}$ to the Minkowski metric at a point of the spacetime, which is always possible because it is equivalent to make diagonal a symmetric matrix with constant coefficients and then rescale the coordinates to reduce the diagonal elements to ± 1. See, for example, Ref. [41] for more details.

[19] Please note the notation adopted in this tutorial. ω is used to indicate a generic angular velocity, while the Keplerian angular velocity of the material in the disk is indicated by $\Omega_{\rm K}$ and the angular velocity of a locally non-rotating reference frame is indicated by $\Omega_{\rm LNRF}$.

[20] From Equation (14) we see that a particle with $L_z = 0$ has a non-vanishing angular velocity in the coordinate system (t, r, θ, ϕ): $d\phi/dt = \dot{\phi}/\dot{t} = -g_{t\phi}/g_{\phi\phi}$. A locally non-rotating observer is thus an observer with vanishing L_z and its non-vanishing angular momentum is due to the frame dragging of the spacetime.

References

1. Page, D.N.; Thorne, K.S. Disk-Accretion onto a Black Hole. Time-Averaged Structure of Accretion Disk. *Astrophys. J.* **1974**, *191*, 499–506. [CrossRef]
2. Shakura, N.I.; Sunyaev, R.A. Black holes in binary systems. Observational appearance. *Astron. Astrophys.* **1973**, *24*, 337–355.

3. Bisnovatyi-Kogan, G.S.; Blinnikov, S.I. Disk accretion onto a black hole at subcritical luminosity. *Astron. Astrophys.* **1977**, *59*, 111–125.
4. Dove, J.B.; Wilms, J.; Maisack, M.; Begelman, M.C. Self-consistent thermal accretion disk corona models for compact objects. 2. Application to cygnus x-1. *Astrophys. J.* **1997**, *487*, 759. [CrossRef]
5. Haardt, F.; Maraschi, L.A.M.U. A two-phase model for the X-ray emission from Seyfert galaxies. *Astrophys. J. Lett.* **1991**, *380*, L51–L54. [CrossRef]
6. Liu, B.F.; Mineshige, S.; Ohsuga, K. Spectra from a magnetic reconnection-heated corona in agn. *Astrophys. J.* **2003**, *587*, 571–579. [CrossRef]
7. Markoff, S.; Nowak, M.A.; Wilms, J. Going with the flow: Can the base of jets subsume the role of compact accretion disk coronae? *Astrophys. J.* **2005**, *635*, 1203–1216. [CrossRef]
8. Petrucci, P.O.; Paltani, S.; Malzac, J.; Kaastra, J.S.; Cappi, M.; Ponti, G.; De Marco, B.; Kriss, G.A.; Steenbrugge, K.C.; Bianchi, S.; et al. Multiwavelength campaign on Mrk 509 XII. Broad band spectral analysis. *Astron. Astrophys.* **2013**, *549*, A73. [CrossRef]
9. Sironi, L.; Beloborodov, A.M. Kinetic Simulations of Radiative Magnetic Reconnection in the Coronae of Accreting Black Holes. *Astrophys. J.* **2020**, *899*, 52. [CrossRef]
10. Titarchuk, L. Generalized Comptonization models and application to the recent high-energy observations. *Astrophys. J.* **1994**, *434*, 570–586. [CrossRef]
11. Kara, E.; Steiner, J.F.; Fabian, A.C.; Cackett, E.M.; Uttley, P.; Remillard, R.A.; Gendreau, K.C.; Arzoumanian, Z.; Altamirano, D.; Eikenberry, S.; et al. The corona contracts in a black-hole transient. *Nature* **2019**, *565*, 198. [CrossRef] [PubMed]
12. Dai, X.; Kochanek, C.S.; Chartas, G.; Kozlowski, S.; Morgan, C.W.; Garmire, G.; Agol, E. The Sizes of the X-ray and Optical Emission Regions of RXJ1131-1231. *Astrophys. J.* **2010**, *709*, 278–285. [CrossRef]
13. Wilkins, D.R.; Gallo, L.C. Driving extreme variability: The evolving corona and evidence for jet launching in Markarian 335. *Mon. Not. R. Astron. Soc.* **2015**, *449*, 129–146. [CrossRef]
14. Zdziarski, A.A.; Johnson, W.N.; Magdziarz, P. Broad-band gamma-ray and x-ray spectra of ngc 4151 and their implications for physical processes and geometry. *Mon. Not. R. Astron. Soc.* **1996**, *283*, 193. [CrossRef]
15. Zdziarski, A.A.; Szanecki, M.; Poutanen, J.; Gierlinski, M.; Biernacki, P. Spectral and temporal properties of Compton scattering by mildly relativistic thermal electrons. *Mon. Not. R. Astron. Soc.* **2020**, *492*, 5234–5246. [CrossRef]
16. Bambi, C. Black hole X-ray spectra: Notes on the relativistic calculations. *arXiv* **2024**, arXiv:2408.12262.
17. Garcia, J.; Kallman, T. X-ray reflected spectra from accretion disk models. I. Constant density atmospheres. *Astrophys. J.* **2010**, *718*, 695. [CrossRef]
18. Ross, R.R.; Fabian, A.C. A Comprehensive range of x-ray ionized reflection models. *Mon. Not. R. Astron. Soc.* **2005**, *358*, 211–216. [CrossRef]
19. Bambi, C. *Black Holes: A Laboratory for Testing Strong Gravity*; Springer: Singapore, 2017; ISBN 978-981-10-4524-0. [CrossRef]
20. Fabian, A.C.; Rees, M.J.; Stella, L.; White, N.E. X-ray fluorescence from the inner disc in Cygnus X-1. *Mon. Not. R. Astron. Soc.* **1989**, *238*, 729–736. [CrossRef]
21. Kojima, Y. The effects of black hole rotation on line profiles from accretion discs. *Mon. Not. R. Astron. Soc.* **1991**, *250*, 629. [CrossRef]
22. Laor, A. Line profiles from a disk around a rotating black hole. *Astrophys. J.* **1991**, *376*, 90. [CrossRef]
23. Bambi, C.; Brenneman, L.W.; Dauser, T.; Garcia, J.A.; Grinberg, V.; Ingram, A.; Jiang, J.; Liu, H.; Lohfink, A.M.; Marinucci, A.; et al. Towards Precision Measurements of Accreting Black Holes Using X-Ray Reflection Spectroscopy. *Space Sci. Rev.* **2021**, *217*, 65. [CrossRef]
24. Brenneman, L.W.; Reynolds, C.S. Constraining Black Hole Spin Via X-ray Spectroscopy. *Astrophys. J.* **2006**, *652*, 1028–1043. [CrossRef]
25. Draghis, P.A.; Miller, J.M.; Costantini, E.; Gallo, L.C.; Reynolds, M.; Tomsick, J.A.; Zoghbi, A. Systematically Revisiting All NuSTAR Spins of Black Holes in X-Ray Binaries. *Astrophys. J.* **2024**, *969*, 40. [CrossRef]
26. Cao, Z.; Nampalliwar, S.; Bambi, C.; Dauser, T.; Garcia, J.A. Testing general relativity with the reflection spectrum of the supermassive black hole in 1H0707-495. *Phys. Rev. Lett.* **2018**, *120*, 51101. [CrossRef]
27. Tripathi, A.; Nampalliwar, S.; Abdikamalov, A.B.; Ayzenberg, D.; Bambi, C.; Dauser, T.; Garcia, J.A.; Marinucci, A. Toward Precision Tests of General Relativity with Black Hole X-Ray Reflection Spectroscopy. *Astrophys. J.* **2019**, *875*, 56. [CrossRef]
28. Tripathi, A.; Zhang, Y.; Abdikamalov, A.B.; Ayzenberg, D.; Bambi, C.; Jiang, J.; Liu, H.; Zhou, M. Testing General Relativity with NuSTAR data of Galactic Black Holes. *Astrophys. J.* **2021**, *913*, 79. [CrossRef]
29. Papapetrou, A. Champs gravitationnels stationnaires a symetrie axiale. *Ann. Inst. H. Poincare Phys. Theor.* **1966**, *4*, 83–105.
30. Wald, R.M. *General Relativity*; Chicago University Press: Chicago, IL, USA, 1984. [CrossRef]
31. Lindquist, R.W. Relativistic transport theory. *Ann. Phys.* **1966**, *37*, 487–518. [CrossRef]
32. Bambi, C.; Malafarina, D.; Tsukamoto, N. Note on the effect of a massive accretion disk in the measurements of black hole spins. *Phys. Rev. D* **2014**, *89*, 127302. [CrossRef]
33. Balbus, S.A.; Hawley, J.F. A powerful local shear instability in weakly magnetized disks. 1. Linear analysis. 2. Nonlinear evolution. *Astrophys. J.* **1991**, *376*, 214–233. [CrossRef]
34. Bardeen, J.M.; Press, W.H.; Teukolsky, S.A. Rotating black holes: Locally nonrotating frames, energy extraction, and scalar synchrotron radiation. *Astrophys. J.* **1972**, *178*, 347. [CrossRef]

35. Bambi, C.; Barausse, E. The Final stages of accretion onto non-Kerr compact objects. *Phys. Rev. D* **2011**, *84*, 84034. [CrossRef]
36. Bambi, C.; Lukes-Gerakopoulos, G. Testing the existence of regions of stable orbits at small radii around black hole candidates. *Phys. Rev. D* **2013**, *87*, 83006. [CrossRef]
37. Shashank, S.; Riaz, S.; Abdikamalov, A.B.; Bambi, C. Testing Relativistic Reflection Models with GRMHD Simulations of Accreting Black Holes. *Astrophys. J.* **2022**, *938*, 53. [CrossRef]
38. Riaz, S.; Abdikamalov, A.B.; Ayzenberg, D.; Bambi, C.; Wang, H.; Yu, Z. Reflection Spectra of Accretion Disks Illuminated by Disk-like Coronae. *Astrophys. J.* **2022**, *925*, 51. [CrossRef]
39. Dauser, T.; Garcia, J.; Wilms, J.; Bock, M.; Brenneman, L.W.; Falanga, M.; Fukumura, K.; Reynolds, C.S. Irradiation of an Accretion Disc by a Jet: General Properties and Implications for Spin Measurements of Black Holes. *Mon. Not. R. Astron. Soc.* **2013**, *430*, 1694. [CrossRef]
40. Fukumura, K.; Kazanas, D. Accretion Disk Illumination in Schwarzschild and Kerr Geometries: Fitting Formulae. *Astrophys. J.* **2007**, *664*, 14–25. [CrossRef]
41. Bambi, C. *Introduction to General Relativity*; Springer: Singapore, 2018; ISBN 978-981-13-1089-8/978-981-13-1090-4. [CrossRef]
42. Bambi, C. Search for Variations of Fundamental Constants in the book. In *Recent Progress on Gravity Tests: Challenges and Future Perspectives*; Bambi, C., Cardenas-Avendano, A., Eds.; Springer: Singapore, 2024; pp. 417–432. [CrossRef]
43. Mirzaev, T.; Riaz, S.; Abdikamalov, A.B.; Bambi, C.; Dauser, T.; Garcia, J.A.; Jiang, J.; Liu, H.; Shashank, S. Toward More Accurate Synthetic Reflection Spectra: Improving the Calculations of Returning Radiation. *Astrophys. J.* **2024**, *965*, 66. [CrossRef]
44. Mirzaev, T.; Bambi, C.; Abdikamalov, A.B.; Jiang, J.; Liu, H.; Riaz, S.; Shashank, S. X-Ray Spectra of Black Hole X-Ray Binaries with Returning Radiation. *Astrophys. J.* **2024**, *976*, 229. [CrossRef]
45. Luminet, J.P. Image of a spherical black hole with thin accretion disk. *Astron. Astrophys.* **1979**, *75*, 228–235.
46. Reynolds, C.S.; Begelman, M.C. Iron fluorescence from within the innermost stable orbit of black hole accretion disks. *Astrophys. J.* **1997**, *488*, 109. [CrossRef]
47. García, J.; Dauser, T.; Lohfink, A.; Kallman, T.R.; Steiner, J.; McClintock, J.E.; Brenneman, L.; Wilms, J.; Eikmann, W.; Reynolds, C.S.; et al. Improved Reflection Models of Black-Hole Accretion Disks: Treating the Angular Distribution of X-rays. *Astrophys. J.* **2014**, *782*, 76. [CrossRef]
48. Novikov, I.D.; Thorne, K.S. Astrophysics of Black Holes. In *Black Holes*; De Witt, C., De Witt, B., Eds.; Gordon and Breach: New York, NY, USA, 1973; pp. 343–450.
49. Davis, S.W.; Blaes, O.M.; Hubeny, I.; Turner, N.J. Relativistic accretion disk models of high state black hole x-ray binary spectra. *Astrophys. J.* **2005**, *621*, 372–387. [CrossRef]
50. Davis, S.W.; Hubeny, I. A grid of relativistic, non-lte accretion disk models for spectral fitting of black hole binaries. *Astrophys. J. Suppl.* **2006**, *164*, 530. [CrossRef]
51. Shimura, T.; Takahara, F. On the spectral hardening factor of the X-ray emission from accretion disks in black hole candidates. *Astrophys. J.* **1995**, *445*, 780–788. [CrossRef]
52. Miller, J.M.; Fabian, A.C.; Kaastra, J.; Kallman, T.; King, A.L.; Proga, D.; Raymond, J.; Reynolds, C.S. Powerful, Rotating Disk Winds from Stellar-mass Black Holes. *Astrophys. J.* **2015**, *814*, 87. [CrossRef]
53. Mummery, A.; Ingram, A.; Davis, S.; Fabian, A. Continuum emission from within the plunging region of black hole discs. *Mon. Not. R. Astron. Soc.* **2024**, *531*, 366–386. [CrossRef]
54. Abdikamalov, A.B.; Ayzenberg, D.; Bambi, C.; Dauser, T.; Garcia, J.A.; Nampalliwar, S.; Tripathi, A.; Zhou, M. Testing the Kerr black hole hypothesis using X-ray reflection spectroscopy and a thin disk model with finite thickness. *Astrophys. J.* **2020**, *899*, 80. [CrossRef]
55. Bambi, C.; Cardenas-Avendano, A.; Dauser, T.; Garcia, J.A.; Nampalliwar, S. Testing the Kerr black hole hypothesis using X-ray reflection spectroscopy. *Astrophys. J.* **2017**, *842*, 76. [CrossRef]
56. Cunningham, C.T. The effects of redshifts and focusing on the spectrum of an accretion disk around a Kerr black hole. *Astrophys. J.* **1975**, *202*, 788–802. [CrossRef]
57. Speith, R.; Riffert, H.; Ruder, H. The photon transfer function for accretion disks around a Kerr black hole. *Comput. Phys. Comm.* **1995**, *88*, 109–120. [CrossRef]
58. Zhou, M.; Abdikamalov, A.B.; Ayzenberg, D.; Bambi, C.; Liu, H.; Nampalliwar, S. XSPEC model for testing the Kerr black hole hypothesis using the continuum-fitting method. *Phys. Rev. D* **2019**, *99*, 104031. [CrossRef]
59. Gonzalez, A.G.; Wilkins, D.R.; Gallo, L.C. Probing the geometry and motion of AGN coronae through accretion disc emissivity profiles. *Mon. Not. R. Astron. Soc.* **2017**, *472*, 1932–1945. [CrossRef]
60. Tripathi, A.; Yan, J.; Yang, Y.; Yan, Y.; Garnham, M.; Yao, Y.; Li, S.; Ding, Z.; Abdikamalov, A.B.; Ayzenberg, D.; et al. Constraints on the Spacetime Metric around Seven "Bare" AGNs Using X-Ray Reflection Spectroscopy. *Astrophys. J.* **2019**, *874*, 135. [CrossRef]
61. Fabian, A.C.; Vaughan, S.; Nandra, K.; Iwasawa, K.; Ballantyne, D.R.; Lee, J.C.; De Rosa, A.; Turner, A.; Young, A.J. A Long hard look at MCG-6-30-15 with XMM-Newton. *Mon. Not. R. Astron. Soc.* **2002**, *335*, L1. [CrossRef]
62. Iwasawa, K.; Fabian, A.C.; Reynolds, C.S.; Nandra, K.; Otani, C.; Inoue, H.; Hayashida, K.; Brandt, W.N.; Dotani, T.; Kunieda, H.; et al. The Variable iron k emission line in MCG-6-30-15. *Mon. Not. R. Astron. Soc.* **1996**, *282*, 1038–1048. [CrossRef]
63. Guainazzi, M.; Matt, G.; Molendi, S.; Orr, A.; Fiore, F.; Grandi, P.; Matteuzzi, A.; Mineo, T.; Perola, G.C.; Parmar, A.N.; et al. BeppoSAX confirms extreme relativistic effects in the X-ray spectrum of MCG-6-30-15. *Astron. Astrophys.* **1999**, *341*, L27.

64. Marinucci, A.; Matt, G.; Miniutti, G.; Guainazzi, M.; Parker, M.L.; Brenneman, L.; Fabian, A.C.; Kara, E.; Arevalo, P.; Ballantyne, D.R.; et al. The Broadband Spectral Variability of MCG–6-30-15 Observed by *NuSTAR* and *XMM-Newton*. *Astrophys. J.* **2014**, *787*, 83. [CrossRef]
65. Miniutti, G.; Fabian, A.C.; Anabuki, N.; Crummy, J.; Fukazawa, Y.; Gallo, L.; Haba, Y.; Hayashida, K.; Holt, S.; Kunieda, H. et al. Suzaku observations of the hard X-ray variability of MCG-6-30-15: The effects of strong gravity around a Kerr black hole. *Publ. Astron. Soc. Jap.* **2007**, *59*, 315. [CrossRef]
66. Tanaka, Y.; Nandra, K.; Fabian, A.C.; Inoue, H.; Otani, C.; Dotani, T.; Hayashida, K.; Iwasawa, K.; Kii, T.; Kunieda, H.; et al. Gravitationally Redshifted Emission Implying an Accretion Disk and Massive Black Hole in the Active Galaxy MCG:-6-30-15. *Nature* **1995**, *375*, 659. [CrossRef]
67. Tripathi, A.; Liu, H.; Bambi, C. Impact of the reflection model on the estimate of the properties of accreting black holes. *Mon. Not. R. Astron. Soc.* **2020**, *498*, 3565–3577. [CrossRef]
68. Kammoun, E.S.; Nardini, E.; Risaliti, G. Testing the accuracy of reflection-based supermassive black hole spin measurements in AGN. *Astron. Astrophys.* **2018**, *614*, A44. [CrossRef]
69. Fabian, A.C.; Parker, M.L.; Wilkins, D.R.; Miller, J.M.; Kara, E.; Reynolds, C.S.; Dauser, T. On the determination of the spin and disc truncation of accreting black holes using X-ray reflection. *Mon. Not. R. Astron. Soc.* **2014**, *439*, 2307–2313. [CrossRef]
70. Steiner, J.F.; McClintock, J.E.; Remillard, R.A.; Gou, L.; Yamada, S.; Narayan, R. The Constant Inner-Disk Radius of LMC X-3: A Basis for Measuring Black Hole Spin. *Astrophys. J. Lett.* **2010**, *718*, L117–L121. [CrossRef]
71. Tripathi, A.; Abdikamalov, A.B.; Ayzenberg, D.; Bambi, C.; Liu, H. Impact of the Disk Thickness on X-Ray Reflection Spectroscopy Measurements. *Astrophys. J.* **2021**, *913*, 129. [CrossRef]
72. Riaz, S.; Ayzenberg, D.; Bambi, C.; Nampalliwar, S. Reflection spectra of thick accretion discs. *Mon. Not. R. Astron. Soc.* **2020**, *491*, 417–426. [CrossRef]
73. Riaz, S.; Ayzenberg, D.; Bambi, C.; Nampalliwar, S. Modeling bias in supermassive black hole spin measurements. *Astrophys. J.* **2020**, *895*, 61. [CrossRef]
74. Wilkins, D.R.; Fabian, A.C. Determination of the X-ray reflection emissivity profile of 1H 0707-495. *Mon. Not. R. Astron. Soc.* **2011**, *414*, 1269–1277. [CrossRef]
75. Reynolds, C.S.; Fabian, A.C. Broad iron K-alpha emission lines as a diagnostic of black hole spin. *Astrophys. J.* **2008**, *675*, 1048. [CrossRef]
76. Cardenas-Avendano, A.; Zhou, M.; Bambi, C. Modeling uncertainties in X-ray reflection spectroscopy measurements II: Impact of the radiation from the plunging region. *Phys. Rev. D* **2020**, *101*, 123014. [CrossRef]
77. Li, L.X.; Zimmerman, E.R.; Narayan, R.; McClintock, J.E. Multi-temperature blackbody spectrum of a thin accretion disk around a Kerr black hole: Model computations and comparison with observations. *Astrophys. J. Suppl.* **2005**, *157*, 335–370. [CrossRef]
78. Dauser, T.; Garc, J.A.; Joyce, A.; Lickleder er, S.; Connors, R.M.T.; Ingram, A.; Reynolds, C.S.; Wilms, J. The effect of returning radiation on relativistic reflection. *Mon. Not. R. Astron. Soc.* **2022**, *514*, 3965–3983. [CrossRef]
79. Tashiro, M.; Maejima, H.; Toda, K.; Kelley, R.; Reichenthal, L.; Hartz, L.; Petre, R.; Williams, B.; Guainazzi, M.; Costantini, E.; et al. Status of x-ray imaging and spectroscopy mission (XRISM). *Proc. SPIE Int. Soc. Opt. Eng.* **2020**, *11444*, 1144422. [CrossRef]
80. Barret, D.; Trong, T.L.; Herder, J.W.D.; Piro, L.; Barcons, X.; Huovelin, J.; Kelley, R.; Mas-Hesse, J.M.; Mitsuda, K.; Paltani, S.; et al. The Athena X-ray Integral Field Unit (X-IFU). *Proc. SPIE Int. Soc. Opt. Eng.* **2016**, *9905*, 99052F. [CrossRef]